Recent advances on the fast multipole accelerated boundary element method for 3D time-harmonic elastodynamics

Stéphanie Chaillat, Marc Bonnet

▶ To cite this version:

HAL Id: hal-00805764

https://hal.archives-ouvertes.fr/hal-00805764

Submitted on 28 Mar 2013

Recent advances on the fast multipole accelerated boundary element method for 3D time-harmonic elastodynamics[*]

Stéphanie CHAILLAT, Marc BONNET
POems (UMR 7231 CNRS-ENSTA-INRIA), ENSTA, Paris, France
stephanie.chaillat@ensta.fr, marc.bonnet@ensta.fr

Abstract

This article is mainly devoted to a review on fast BEMs for elastodynamics, with particular attention on time-harmonic fast multipole methods (FMMs). It also includes original results that complete a very recent study on the FMM for elastodynamic problems in semi-infinite media. The main concepts underlying fast elastodynamic BEMs and the kernel-dependent elastodynamic FM-BEM based on the diagonal-form kernel decomposition are reviewed. An elastodynamic FM-BEM based on the half-space Green's tensor suitable for semi-infinite media, and in particular on the fast evaluation of the corresponding governing double-layer integral operator involved in the BIE formulation of wave scattering by underground cavities, is then presented. Results on numerical tests for the multipole evaluation of the half-space traction Green's tensor and the FMM treatment of a sample 3D problem involving wave scattering by an underground cavity demonstrate the accuracy of the proposed approach. The article concludes with a discussion of several topics open to further investigation, with relevant published work surveyed in the process.

1 Introduction

The boundary element method (BEM), pioneered in the sixties as a numerical solution methodology, results from the discretization of boundary integral equation (BIE) formulations. The latter are known since a long time for many classical problems of physics such as electricity and magnetism, heat transfer, fluid flow, mechanics of deformable solids... As it exploits the conversion of partial differential equations supported on domains to integral equations supported on domain boundaries, the BEM is a mesh reduction method, subject to restrictive constitutive assumptions but yielding highly accurate solutions. The reader is referred to the recent review article [54] for an abundant bibliography on the general topic of BIE/BEM formulations which includes historical aspects and recent developments, see also [11, 13].

BEMs are in particular well suited to dealing with unbounded-domain idealizations, since computations on large domains are condensated on its boundary. Such idealizations are for example commonly used for computations involving electric or magnetic fields, which arise in the surrounding air or vacuum as well as inside solid materials, and also in many situations involving (electromagnetic, acoustic, elastic) waves. What makes BIE formulations well suited to configurations involving infinite media is the fact that integral representation formulae automatically verify decay or radiation conditions. BEMs thus constitute an appealing alternative to domain discretization methods for wave propagation problems, as artificial boundary conditions [7] are not required for dealing with the radiation conditions, and grid dispersion cumulative effects are absent [45].

The theory of BIE formulations for elastic waves and the resulting basic BIE formulations have been known since several decades, see e.g. [1, 32, 51]. As a result, BEMs for elastodynamics appeared over four decades ago [26]. They have hence been the subject of sustained research and applications, as witnessed by e.g. the review article [12]. The modelling of waves propagating in soils and geological structures, with applications in geophysics, seismology or civil engineering, often resorts to BEMs, sometimes in association with FEMs or other methods [24, 63, 71].

In traditional boundary element (BE) implementations, the dimensional (and induced mesh reduction) advantage with respect to domain discretization methods is offset by the fully-populated nature of the BEM coefficient matrix, which results in computational work and memory requirement that grow rapidly with the problem size N; in other words, the high complexity of traditional BEMs precludes its application to large models. This severe limitation has prompted the development of alternative, faster solution strategies that allow to still exploit the known advantages of BEMs when large N rules out its use in standard form. Fast BEMs, i.e. BEMs of complexity lower than that of traditional BEMs, appeared in [65], where a fast multipole method (FMM) is proposed for solving 2-D Laplace problems within $O(N)$ CPU time per iteration. The scope and capabilities of fast multipole boundary element methods (FM-BEMs) thereafter rapidly progressed, especially in connection with applications in electromagnetics [55, 75], but also in other fields including acoustics(e.g. [68, 70]) and computational mechanics (e.g. [53]). Many of the early investigations are surveyed in the review article [62]. The FMM, as well as other fast BEM approaches [10, 81, 85], relies upon an iterative solution approach for the linear system of discretized BEM equations, with solution times typically of order $O(N \log N)$ per iteration for frequency-domain wave propagation problems (instead of $O(N^2)$ per iteration with traditional forms of the BEM).

This article is mainly devoted to a review on fast BEMs for elastodynamics, with particular attention on fast multipole methods for time-harmonic problems, while also including some original results that follow up a very recent study on a new FMM for elastodynamic problems in semi-infinite media [18], a configuration for which no FM-BEM was previously available. It is organised as follows. Background material is gathered in the remainder of this section. The main concepts underlying fast elastodynamic BEMs and the kernel-dependent elastodynamic FM-BEM based on the diagonal-form kernel decomposition are reviewed in Sections 2 and 3, respectively. Section 4 is then devoted to a FM-BEM based on the half-space Green's tensor suitable for semi-infinite media, with emphasis on the fast evaluation of the corresponding governing double-layer integral operator involved in the BIE formulation of wave scattering by underground cavities. Results on numerical tests on the multipole evaluation of the half-space traction Green's tensor and on a sample 3D scattering problem are presented. Finally, Section 5 discusses several issues deserving further investigation and surveys relevant published work in the process.

1.1 Frequency-domain BIE formulation

Integral representation. The BIE formulation for frequency-domain elastodynamics is now summarized in its basic form, as it defines a convenient framework and notational setting for starting the discussion of fast BEMs for elastodynamics. Accordingly, let $\Omega \subset \mathbb{R}^3$ denote the region of space occupied by a three-dimensional elastic solid with constitutive properties defined by the fourth-order elasticity tensor $\mathbfcal{C}$ and the mass density ρ. Assume for definiteness that time-harmonic motions, with circular frequency ω, are induced by a

prescribed traction distribution $\boldsymbol{t}^{\mathrm{D}}$ on the boundary $\partial\Omega$ and in the absence of body forces (with straightforward modifications allowing the discussion of other boundary conditions or other integral formulations). The displacement $\boldsymbol{u}$ is given at an interior point $\boldsymbol{x} \in \Omega$ by the following well-known representation formula [32]:

$$\boldsymbol{u}(\boldsymbol{x}) = -\int_{\partial\Omega} \boldsymbol{u}(\boldsymbol{y}){\cdot}\boldsymbol{T}(\boldsymbol{x},\boldsymbol{y})\,\mathrm{d}S_y + \int_{\partial\Omega} \boldsymbol{t}^{\mathrm{D}}(\boldsymbol{y}){\cdot}\boldsymbol{U}(\boldsymbol{x},\boldsymbol{y})\,\mathrm{d}S_y \qquad (\boldsymbol{x} \in \Omega), \tag{1}$$

where $\boldsymbol{U}(\boldsymbol{x},\boldsymbol{y})$ and $\boldsymbol{T}(\boldsymbol{x},\boldsymbol{y})$ denote an elastodynamic Green's tensor, defined such that $\boldsymbol{U}{\cdot}\boldsymbol{F}$ and $\boldsymbol{T}{\cdot}\boldsymbol{F}$ are the displacement and traction vector, respectively, generated at any point $\boldsymbol{y}$ of a region $\mathcal{O} \subset \mathbb{R}^3$ by a unit point force $\boldsymbol{F}$ applied at $\boldsymbol{x} \in \mathcal{O}$. The region $\mathcal{O}$ must contain Ω, and many Green's tensors may then be defined according to the choice of $\mathcal{O} \supset \Omega$ and boundary conditions on $\partial\mathcal{O}$ (later in this article, the case where $\mathcal{O}$ is a half-space with traction-free conditions on $\partial\mathcal{O}$ will be considered). The simplest, and most commonly used, Green's tensor corresponds to the isotropic full-space, i.e. $\mathcal{O} = \mathbb{R}^3$ and

$$\boldsymbol{\mathcal{C}} = 2\mu\Big[\frac{\nu}{1-2\nu}\boldsymbol{I}\otimes\boldsymbol{I} + \boldsymbol{\mathcal{I}}\Big], \tag{2}$$

where μ and ν are the shear modulus and the Poisson's ratio of the material, $\boldsymbol{I}$ being the second-order identity tensor and $\boldsymbol{\mathcal{I}}$ the symmetric fourth-order identity tensor. In this case, one has [32]:

$$\boldsymbol{U}(\boldsymbol{x},\boldsymbol{y}) = \frac{1}{k_{\mathrm{S}}^2\mu}\Big[\big(\boldsymbol{I}\Delta - \boldsymbol{\nabla}_y\boldsymbol{\nabla}_x\big)G(|\boldsymbol{y}-\boldsymbol{x}|;k_{\mathrm{S}}) + \boldsymbol{\nabla}_x\boldsymbol{\nabla}_y G(|\boldsymbol{y}-\boldsymbol{x}|;k_{\mathrm{P}})\Big],$$

$$\boldsymbol{T}(\boldsymbol{x},\boldsymbol{y}) = \boldsymbol{n}(\boldsymbol{y}){\cdot}\boldsymbol{\mathcal{C}}{:}\boldsymbol{\nabla}_y\boldsymbol{U}(\boldsymbol{x},\boldsymbol{y}), \tag{3}$$

where $\boldsymbol{n}(\boldsymbol{y})$ is the unit normal to $\partial\Omega$ directed outwards of Ω; k_{S} and k_{P} are the respective wavenumbers of S and P elastic waves, so that

$$k_{\mathrm{S}}^2 = \frac{\rho\omega^2}{\mu}, \quad k_{\mathrm{P}} = \kappa k_{\mathrm{S}}, \qquad \text{with } \kappa^2 = \frac{1-2\nu}{2(1-\nu)}; \tag{4}$$

and $G(\cdot;k)$ is the free-space fundamental solution for the Helmholtz equation with wavenumber k, given by

$$G(r;k) = \frac{\exp(\mathrm{i}kr)}{4\pi r}. \tag{5}$$

Boundary integral equation. Well-known results on the limiting values of elastic potentials as the collocation point $\boldsymbol{x}$ reaches the boundary [51] allow to deduce from (1) the boundary integral equation

$$\mathcal{K}[\boldsymbol{u}](\boldsymbol{x}) = \mathcal{S}[\boldsymbol{t}^{\mathrm{D}}](\boldsymbol{x}) \quad (\boldsymbol{x} \in \partial\Omega) \qquad \text{with } \mathcal{K}[\boldsymbol{u}](\boldsymbol{x}) := \mathcal{D}[\boldsymbol{u}](\boldsymbol{x}) + \boldsymbol{c}(\boldsymbol{x}){\cdot}\boldsymbol{u}(\boldsymbol{x}), \tag{6}$$

where the right-hand side and the linear operator $\mathcal{K}$ respectively involve the single-layer integral operator $\mathcal{S}$ and the double-layer integral operator $\mathcal{D}$, defined by

$$\mathcal{S}[\boldsymbol{t}](\boldsymbol{x}) := \int_{\partial\Omega} \boldsymbol{t}(\boldsymbol{y}){\cdot}\boldsymbol{U}(\boldsymbol{x},\boldsymbol{y})\,\mathrm{d}S_y, \quad \mathcal{D}[\boldsymbol{u}](\boldsymbol{x}) := (\mathrm{P.V.})\int_{\partial\Omega} \boldsymbol{u}(\boldsymbol{y}){\cdot}\boldsymbol{T}(\boldsymbol{x},\boldsymbol{y})\,\mathrm{d}S_y \tag{7}$$

Due to the strong singularity of $\boldsymbol{T}$ for $\boldsymbol{y} = \boldsymbol{x}$, the integral defining $\mathcal{D}$ is understood in the Cauchy principal value (CPV) sense (as indicated by the notation P.V.) while a *free-term* $\boldsymbol{c}(\boldsymbol{x})$ arose from the limit-to-the-boundary process. The latter is equal to $0.5\boldsymbol{I}$ (with $\boldsymbol{I}$ denoting the second-order identity tensor) in the usual case where $\partial\Omega$ is smooth at $\boldsymbol{x}$, and is otherwise a known (second-order tensor-valued) function of the local geometry of $\partial\Omega$ at $\boldsymbol{x}$. Kernel singularities are extensively studied in the literature in terms of their

consequences on the fundamental properties of integral operators [61] and the specialized numerical quadrature methods allowing to handle them in implementing the BEM [80].

1.2 Boundary element method

The numerical solution of boundary integral equation (6) is based on a discretization of the surface $\partial\Omega$ into boundary elements. This discretization process, either based on nodal collocation or on a Galerkin approach, transforms (6) into a square complex-valued matrix equation of the form

$$\mathbf{Ku} = \mathbf{f}, \tag{8}$$

where the N-vector $\mathbf{u}$ collects the sought degrees of freedom (DOFs), namely the nodal displacement components, $\mathbf{K}$ is the $N \times N$ influence matrix and the N-vector $\mathbf{f}$ arises from the discretization of $\boldsymbol{\mathcal{S}}[\boldsymbol{t}^{\mathrm{D}}]$. Setting up the matrix $\mathbf{K}$ classically requires the computation of all element integrals for each collocation point, or of double integrals over all products of elements in the Galerkin approach, thus needing a computational time of order $O(N^2)$.

The influence matrix $\mathbf{K}$ is fully-populated. Usual direct solvers, such as the LU factorization, then require $O(N^3)$ arithmetic operations (i.e. they have a $O(N^3)$ complexity) and $O(N^2)$ memory, limiting the applicability of the traditional BEM to moderately-sized models (with typically $N = O(10^4)$ or less using double-precision complex arithmetic). BEM problems of larger size are preferably solved by means of iterative algorithms (GMRES [66] being the usual choice), which build sequences $(\mathbf{u}^{(k)})_{k\in\mathbb{N}}$ of solution candidates until $\|\mathbf{Ku}^{(k)} - \mathbf{f}\|/\|\mathbf{f}\|$ is less that a predefined tolerance. Each GMRES iteration requires one evaluation of $\mathbf{Kw}$ for given $\mathbf{w}$, a task of computational complexity $O(N^2)$ whether $\mathbf{K}$ is set up and stored prior to the iterations, or $\mathbf{Kw}$ is evaluated directly by means of standard BEM numerical integration and assembly procedures. In the latter case, the $O(N^2)$ complexity results from the need to compute all element integrals for each collocation point.

2 Fast BEMs for frequency-domain elastodynamics

Applications of the BEM to large models (typically at least $N = O(10^6)$) require evaluation procedures for $\mathbf{Kw}$ whose complexity is lower than $O(N^2)$ and which do not require explicit setup and storage of $\mathbf{K}$. Several approaches, collectively referred to as fast BEMs, have been proposed and developed towards meeting these requirements on complexity. They are reviewed in this section, with emphasis on application to elastodynamics. One notes that $\mathbf{w} \to \mathbf{Kw}$ is (up to the additive free term) a discretized version of the double-layer integral operator $\boldsymbol{w} \to \boldsymbol{\mathcal{D}}[\boldsymbol{w}]$, so that fast BEMs essentially consist in accelerated methods for the evaluation of discretized integral operators on given densities. The standard BIE formulation (6) applied to exterior problems is known to break down when ω is a so-called fictitious eigenvalue. Fast integral operator evaluation methods discussed here do nothing by themselves to remedy this issue. They may however be derived and applied to other BIE formulations which are immune to fictitious eigenvalues such as that of Burton and Miller, see e.g. [27].

To reduce the complexity incurred by matrix-vector products $\mathbf{Kw}$, one needs to define an approximation $\mathbf{K}_\varepsilon$ of $\mathbf{K}$ such that (a) $\|\mathbf{K} - \mathbf{K}_\varepsilon\| \le \varepsilon\|\mathbf{K}\|$ (where ε is a preset desired relative accuracy) and (b) $\mathbf{K}_\varepsilon$ is increasingly sparse as N grows, so that the computational cost of evaluating good approximations $\mathbf{K}_\varepsilon\mathbf{w}$ of $\mathbf{Kw}$ grows at a rate lower than $O(N^2)$. The fast BEMs essentially differ in how $\mathbf{K}_\varepsilon$ is defined.

4

FMM based on explicit kernel decomposition. The FMM consists in formulating sparse approximations of integral operators such as $\mathcal{K}$ by recasting the fundamental solutions, e.g. $\boldsymbol{U}(\boldsymbol{x}, \boldsymbol{y})$, $\boldsymbol{T}(\boldsymbol{x}, \boldsymbol{y})$ in (1), in terms of products of functions of $\boldsymbol{x}$ and of $\boldsymbol{y}$. On recasting the position vector $\boldsymbol{r} = \boldsymbol{y} - \boldsymbol{x}$ in the form $\boldsymbol{r} = \tilde{\boldsymbol{y}} - \tilde{\boldsymbol{x}} + \boldsymbol{r}_0$, having set $\tilde{\boldsymbol{y}} := \boldsymbol{y} - \boldsymbol{y}_0$, $\tilde{\boldsymbol{x}} := \boldsymbol{x} - \boldsymbol{x}_0$ and $\boldsymbol{r}_0 := \boldsymbol{y}_0 - \boldsymbol{x}_0$ in terms of two chosen poles $\boldsymbol{x}_0$, $\boldsymbol{y}_0$ (Fig. 1), decompositions of the form

$$K(\boldsymbol{x}, \boldsymbol{y}) = \sum_{n=1}^{p} T_n(\boldsymbol{r}_0) X_n(\tilde{\boldsymbol{x}}) Y_n(\tilde{\boldsymbol{y}}) + E(p), \tag{9}$$

called separated decompositions, are sought for generic fundamental solutions $K(\boldsymbol{x}, \boldsymbol{y})$ (with $E(p)$ denoting the truncation error). Selecting a truncation level p such that $E(p) < \varepsilon$ and substituting the above kernel approximation into the relevant integral operators, the resulting BE-discretized influence matrix $\mathbf{K}_\varepsilon$ is seen to be of rank at most p. The desired sparsity of $\mathbf{K}_\varepsilon$ is thus achieved if p is small enough. Note also that the separated character of expansion (9) allows to re-use integrations with respect to $\boldsymbol{y}$ when the collocation point $\boldsymbol{x}$ is changed. This defining feature of the FMM is one of the main mechanisms for lowering the $O(N^2)$ complexity per iteration entailed by standard BEMs, and was in particular at the heart of the original fast summation method for electrostatics [41] (wherein $K(\boldsymbol{x}, \boldsymbol{y}) = C\|\boldsymbol{y} - \boldsymbol{x}\|^{-1}$).

The truncation error $E(p)$ is in general such that it is controllable, and moderate values of p sufficient (i.e low-rank approximations of K are accurate enough), when $\|\tilde{\boldsymbol{x}}\|$, $\|\tilde{\boldsymbol{y}}\|$ are sufficiently small compared to $\|\boldsymbol{r}_0\|$ (e.g. $\|\tilde{\boldsymbol{x}} - \tilde{\boldsymbol{y}}\| / \|\boldsymbol{r}_0\| \leq 2/\sqrt{5}$ for the Helmholtz-type kernels of frequency-domain acoustics or elastodynamics). This naturally lead to subdividing the (collocation, integration) points involved in the BE-discretized integral equation into clusters and applying decompositions of type (9) to well-separated clusters. This subdivision is usually effected by means of a 3D cubic grid of linear spacing d embedding the geometrical support $\partial\Omega$ of (1), so that $\partial\Omega$ is enclosed in a set of cubic cells. The FMM basically consists in using (9), with the poles $\boldsymbol{x_0}$ and $\boldsymbol{y_0}$ chosen as the cell centers, whenever $\boldsymbol{x}$ and $\boldsymbol{y}$ belong to *non-adjacent* cubic cells. When $\boldsymbol{x}$ and $\boldsymbol{y}$ belong to adjacent cells, the original (i.e. non-separated) definitions of the kernels (e.g. (3) with (5)) are used together with classical BEM element integration techniques. To further improve the computational efficiency of the FM-BEM, standard (i.e. non-FMM) calculations must be confined to the smallest possible spatial regions while retaining the advantage of clustering the computation of influence terms into non-adjacent large groups whenever possible. This is achieved by recursively subdividing cubic cells into eight smaller cubic cells. New pairs of non-adjacent smaller cells, to which expansion (9) is applicable, are thus obtained from the subdivision of pairs of adjacent cells. The cell-subdivision approach is systematized by means of an oct-tree structure of cells. At each level ℓ, the linear cell size is denoted d^ℓ. The level $\ell = 0$, composed of only one cubic cell containing the whole surface $\partial\Omega$, is the tree root. The subdivision process is further repeated until the finest level $\ell = \bar{\ell}$, implicitly defined by a preset subdivision-stopping criterion ($d^{\bar{\ell}} \geq d^{\min}$), is reached. Level-$\bar{\ell}$ cells are usu-
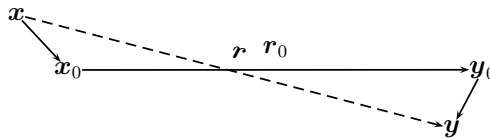

Figure 1: Decomposition of the position vector: notation.

ally termed leaf cells. This octree-based recursive clustering, which defines the so-called multi-level FMM, is the other main mechanism for lowering the complexity of BEMs. The theoretical complexity of the multi-level FMM for Helmholtz-type kernels is in fact known to be $O(N \log N)$ per GMRES iteration both for CPU time and memory [73].

FMMs for (acoustic, electromagnetic, elastic) waves are often based on the fact that the Helmholtz Green's function (5) is known [28, 31] to admit the separated decomposition

$$G(|\boldsymbol{r}|; k) = \lim_{L \to +\infty} G_L(|\boldsymbol{r}|; k), \quad \text{with } G_L(|\boldsymbol{r}|; k) := \int_{\hat{S}} e^{\mathrm{i}k\hat{\boldsymbol{s}}\cdot\tilde{\boldsymbol{y}}} \mathcal{G}_L(\hat{\boldsymbol{s}}; \boldsymbol{r}_0; k) e^{-\mathrm{i}k\hat{\boldsymbol{s}}\cdot\tilde{\boldsymbol{x}}} \, \mathrm{d}\hat{\boldsymbol{s}}, \quad (10)$$

where $\hat{S} \subset \mathbb{R}^3$ is the unit sphere and the *transfer function* $\mathcal{G}_L(\hat{\boldsymbol{s}}; \boldsymbol{r}_0; k)$ is defined in terms of the Legendre polynomials P_n and the spherical Hankel functions of the first kind $h_n^{(1)}$ by:

$$\mathcal{G}_L(\hat{\boldsymbol{s}}; \boldsymbol{r}_0; k) = \frac{\mathrm{i}k}{16\pi^2} \sum_{0 \le n \le L} (2p+1)\mathrm{i}^n h_n^{(1)}(k|\boldsymbol{r}_0|) P_n\big(\cos(\hat{\boldsymbol{s}}, \boldsymbol{r}_0)\big). \quad (11)$$

Replacing the integration over $\hat{S}$ with a numerical quadrature then yields a decomposition of the type (9). Then, since the elastodynamic Green's tensors $\boldsymbol{U}(\boldsymbol{x}, \boldsymbol{y})$, $\boldsymbol{T}(\boldsymbol{x}, \boldsymbol{y})$ given by (3) are linear combinations of derivatives of the Green's function (5), they are amenable to a decomposition similar to (10) [19].

Decomposition (10), often called the diagonal form decomposition of G, is known to fail in the low-frequency limit [28]. Other decompositions that are well-behaved at low frequencies are available, based on either the Gegenbauer addition theorem [87] or Fourier transforms along coordinate planes [40]. So-called wideband FMMs have then be proposed, combining kernel expansions appropriate for low frequencies with the diagonal-form decomposition for higher frequencies [22]. All these approaches are kernel-dependent in that they rely on analytical identities (such as (10) and all representations deriving from it) giving separable decompositions of specific kernels.

A 3D elastodynamic implementation of the low-frequency approach, based on the application of the Gegenbauer addition theorem to G, has been proposed in [86] for the scattering of waves by multiple cracks in unbounded media. Early developments of the diagonal-form decomposition for 3D elastodynamics were presented in [37], with applications to the scattering of seismic waves by basins and topographies. Improved versions of this approach were more recently proposed in [19, 82], with numerical examples involving BE models of size up to $N = O(10^6)$. Moreover, a 2D elastodynamic version of the wideband approach has been recently proposed in [77], while periodic 3D elastodynamic problems are addressed in [46] using a low-frequency separable decomposition of periodic Green's tensors.

Kernel-independent FMM. More recently, kernel decompositions of the form

$$K(\boldsymbol{x}, \boldsymbol{y}) = \sum_{m,n=1}^{p} K(\boldsymbol{x}_m, \boldsymbol{y}_n) I_m(\boldsymbol{x}) I_n(\boldsymbol{y}) + E(p)$$

where I_n is a family of chosen interpolation functions (e.g. Lagrange or Chebyshev polynomials) and $\boldsymbol{x}_m, \boldsymbol{y}_n$ are interpolation nodes, have been investigated [34]. The main conceptual advantage over kernel-dependent decompositions is that the only required knowledge about the kernel is a procedure allowing its evaluation at chosen points. This approach is more recent, and hence less-developed, than the kernel-dependent approach, but oscillatory kernels of type (5) are considered in [30, 59], paving the way to application of this "black-box" approach to elastodynamic FMMs.

Formulations based on the fast Fourier transform (FFT). Another kernel-independent approach exploits the fact that integral operators of convolutional form (i.e. whose kernels are translation-invariant, which includes all full-space fundamental solutions) can be evaluated in $O(N \log N)$ time using the FFT. As in the FMM, an octree is introduced, with each cell discretized into a Cartesian grid that supports FFT operations. Transfers between non-uniform BE meshes and Cartesian grids are effected using sparse anterpolation and interpolation matrices. This approach has been successfully applied to 3D frequency-domain elastodynamics [84] and to a time-frequency treatment of transient elastodynamics [83].

Algebraic methods. A third type of kernel-independent approach for defining a sparse approximation $\mathbf{K}_{\varepsilon}$ of $\mathbf{K}$, is purely algebraic in nature; it is based on the concept of hierarchical matrices, or $\mathcal{H}$-matrices [9]. Here, the influence matrix $\mathbf{K}$ is hierarchically partitioned into blocks in such a way that the lines and columns of the largest blocks correspond to well-separated clusters of collocation and integration nodes (one may note that the octree-based multi-level FMM implicitly defines a hierarchical partition of $\mathbf{K}$). Then, each block is replaced with a low-rank approximation computed using the adaptive cross approximation (ACA) method [10]. Here also, the only required knowledge about the kernel is the ability to evaluate it for any chosen points. Applications of this approach to elastodynamic BEM include [58, 60].

3 Formulations based on the full-space Green's tensor

An initial series of investigations on the elastodynamic FMM [19, 20, 39], whose main features and findings are summarized in this section, has concentrated on the kernel-dependent approach based on the full-space Green's tensor (3).

Single-domain elastodynamic formulation. Multi-level FM-BEM formulations were first considered for single-domain problems, involving (possibly unbounded) homogeneous isotropic elastic media, using integral equations based on the full-space Green's tensor. The acceleration was based on separated decompositions of (3) obtained by substituting decomposition (10) into (3). Many implementation issues arising in this elastodynamic FM-BEM revolve around how to choose the truncation level L in (11) so that (10) is sufficiently accurate. The overall computational cost indeed is strongly dependent on L through not only the number of terms in the transfer function (11), but also the correct number Q of quadrature points on $\hat{S}$, with $Q = O(L^2)$. Selection rules for L in all Helmholtz-type FMMs rest on a key error analysis result [28], which states that there exist four constants C_1, C_2, C_3, C_4 such that

$$L = C_1 + C_2 k |\boldsymbol{r} - \boldsymbol{r}_0| + C_3 \ln(k |\boldsymbol{r} - \boldsymbol{r}_0|) + C_4 \ln \epsilon^{-1} \implies \left| G(|\boldsymbol{r}|; k) - G_L(|\boldsymbol{r}|; k) \right| < \epsilon \quad (12)$$

for any chosen error level $\epsilon < 1$, whenever $\|\boldsymbol{r} - \boldsymbol{r}_0\| / \|\boldsymbol{r}_0\| \leq 2/\sqrt{5}$. First, noting that the magnitude of $\|\boldsymbol{r} - \boldsymbol{r}_0\|$ and $\|\boldsymbol{r}_0\|$ depend on the level (through the linear size of cells for that level), estimate (12) dictates that suitable values of L in (10) are level-dependent. The following selection rule for L (whose form is known from previous studies on FMMs for Maxwell equations [29]), inspired by (12), proved satisfactory:

$$L_\alpha(d) = \sqrt{3} k_\alpha d + C_\epsilon \log_{10}(\sqrt{3} k_\alpha d + \pi), \qquad \alpha = \text{P,S} \quad (13)$$

7

(with d denoting the linear size of a cell, making the rule level-dependent). Note that the recommended value of L depends on whether it is used for the contribution of $G(\cdot; k_P)$ or $G(\cdot; k_S)$ to (3). Empirical tuning of (13) by means of numerical experiments led to set $C_\epsilon = 7.5$ as the best trade-off between accuracy and efficiency.

Moreover, the known low-wavenumber breakdown of decomposition (10), manifested by the $C_2 k|\boldsymbol{r} - \boldsymbol{r}_0|$ contribution in (12), prevents the use of arbitrarily small cells (thus limiting the number of usable levels in the octree). Numerical experiments indicated that the leaf cell size $\bar{d}$ be set so as to verify $\bar{d} \geq 0.6\pi/k_S$.

The version of the elastodynamic FM-BEM incorporating the above-described features was shown (both theoretically and numerically) to conform to the expected $O(N \log N)$ per GMRES iteration computational complexity, and has been validated using a single-CPU desktop computer on test cases involving up to $N = O(10^6)$ BE unknowns.

Multi-domain elastodynamic formulation. The previous treatment has been expanded in [20] so as to allow piecewise-homogeneous media, by coupling integral equations arising from writing (1) separately for each homogeneous component (of course using the Green's tensor with the corresponding material parameters). Then, perfect-bonding transmission conditions were used in weighted combinations of the integral equations obtained for each subdomain, reducing the unknowns to one displacement field and one traction field on each interface. Particular attention needed to be devoted to multiple points (i.e. BE nodes simultaneously belonging to three or more subdomains) and the choice of weighting coefficients. In the resulting implementation of FMM-based BE-BE coupling, surface displacements and tractions are interpolated using piecewise-linear and piecewise-constant functions, respectively (the latter choice of element-based tractions allowing to avoid cumbersome issues related to tractions at multiple points). Contributions from each subdomain to the global matrix-vector product required by the GMRES solver applied to the complete set of equations can be computed by using the single-region elastodynamic FM-BEM in black-box fashion (in particular, octrees are defined separately for each subdomain).

This formulation has been tested on 3D examples including a two-layered semi-spherical basin embedded in an infinite half-space, in particular for the computation of transient responses using Fourier synthesis. The GMRES iteration count was found to be (i) too high for the largest sampling frequencies used and (ii) strongly dependent on the material contrasts between subdomains. These observations highlighted the necessity of addressing the then-current lack of a preconditioning strategy (Sec. 5).

Visco-elastodynamic formulation. The applicability of the single-domain and multi-domain elastodynamic FM-BEM formulations to weakly dissipative visco-elastic media characterized (for fixed frequency) by complex-valued wavenumbers $k_\alpha^\star = k_\alpha(1 + i\zeta_\alpha)$ ($\alpha = $ P,S), where $k_\alpha^\star$ are the elastic pressure and shear wavenumbers and $\zeta_\alpha \ll 1$ are the damping ratios, has been examined in [39]. In particular, the validity of selection rules such as (13) in the complex-wavenumber case, an issue only sparingly addressed in the available literature, was examined. In contrast to the already-mentioned real-wavenumber case, no mathematical error analysis is available. An empirical study based on numerical simulations has shown that a slightly altered version of (13) performs satisfactorily, leading to the adoption of the following damping-dependent selection rule:

$$L_\alpha(d; \zeta_\alpha) = k_\alpha^\star d + (C_\epsilon + C\zeta_\alpha) \log_{10}(k_\alpha^\star d + \pi), \qquad \alpha = \text{P,S} \tag{14}$$

with $C_\epsilon = 7.5$ as before and $C = 60$. This multi-domain visco-elastodynamic FM-BEM has been applied to the problem of a wave propagating in a semi-infinite medium with a lossy semi-spherical inclusion (seismic wave in alluvial basin). Moreover, the semi-infinite configurations considered, typical of applications to soil-structure interaction or seismology, require meshing a portion of the free surface around the irregularities (topography, basins...) considered. In such cases, the potentially large number of additional DOFs required for the free surface and the selection of a suitable truncation radius are serious issues. The latter has been considered through parametric studies using the multi-domain FM-BEM on a semi-spherical basin configuration, with the truncation radius required for making the results reasonably insensitive to truncation found to be of order $13a$ for purely elastic materials (with a denoting the basin radius) while weakly dissipative media allowed to settle for lower values of order $3a - 6a$. Clearly, employing the half-space Green's tensor instead of its (simpler) full-space counterpart used so far would greatly reduce, for a given configuration, the size of the BE model; this approach is addressed next.

4   Formulation based on the elastodynamic half-space Green's tensor

Available (visco)elastodynamic FM-BEMs are to date based on the full-space Green's tensor. However, many applications in e.g. civil engineering or geophysics involve semi-infinite media, and therefore entail a costly BE discretization of a portion of the free surface within a truncation distance that is sufficiently larger than the region of interest (see [6] for the 2D case, where the Rayleigh-wave part of the solution is accounted for beyond the truncation distance). To avoid both this additional computational burden and accuracy control issues raised by the truncation, a natural idea is to use the Green's tensor $\boldsymbol{U}_{\mathrm{HS}}, \boldsymbol{T}_{\mathrm{HS}}$ satisfying the traction-free boundary condition

$$\boldsymbol{T}_{\mathrm{HS}}(\boldsymbol{x}, \boldsymbol{y}) := \boldsymbol{e}_3 \cdot \boldsymbol{\mathcal{C}} \cdot \nabla_y \boldsymbol{U}_{\mathrm{HS}}(\boldsymbol{x}, \boldsymbol{y}) = \boldsymbol{0} \quad (\boldsymbol{y} \in \Gamma_F), \tag{15}$$

on the planar infinite surface $\Gamma_F := \{\boldsymbol{y} \,|\, y_3 = 0\}$ bounding the half-space $\Omega_F := \{\boldsymbol{y} = (y_1, y_2, y_3) \,|\, y_3 < 0\}$ (in (15) and thereafter, the gradient operator $'\boldsymbol{\nabla}'$ conventionally adds one tensorial order from the left, i.e. (for example) $(\boldsymbol{\nabla}\boldsymbol{U})_{kij} = \partial_k U_{ij}$). This choice of Green's tensor is well suited to semi-infinite configurations that feature wave scattering by topographic irregularities or buried objects, modelled as semi-infinite domains Ω which deviate from the half-space Ω_F only in a region of finite size. Here, the boundary $\partial\Omega$ is assumed of the form $\partial\Omega = S \cup \Gamma_0$, where the bounded (and possibly non-connected) surface $S := \partial\Omega \setminus (\partial\Omega \cap \Gamma_F)$ defines topographic irregularities or buried obstacles and $\Gamma_0 \subset \Gamma_F$ is the unbounded planar component of the traction-free surface (Fig. 2). In this setting, the integral equation (6) takes the form (with collocation now needed on S only)

$$\boldsymbol{\mathcal{K}}_{\mathrm{HS}}[\boldsymbol{u}](\boldsymbol{x}) = \boldsymbol{\mathcal{S}}_{\mathrm{HS}}[\boldsymbol{t}^{\mathrm{D}}](\boldsymbol{x}) \quad (\boldsymbol{x} \in S) \tag{16}$$

$$\text{with} \ \ \boldsymbol{\mathcal{K}}_{\mathrm{HS}}[\boldsymbol{u}](\boldsymbol{x}) := \boldsymbol{\mathcal{D}}_{\mathrm{HS}}[\boldsymbol{u}](\boldsymbol{x}) + \boldsymbol{c}(\boldsymbol{x}) \cdot \boldsymbol{u}(\boldsymbol{x}), \tag{17}$$
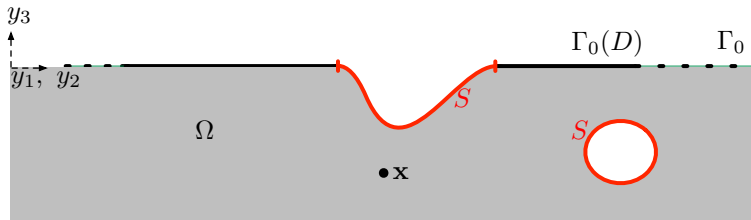

Figure 2: Elastic semi-infinite medium: geometry and notations.

where the single-layer and double-layer integral operators $\mathcal{S}_{\mathrm{HS}}$ and $\mathcal{D}_{\mathrm{HS}}$ defined by

$$\mathcal{S}_{\mathrm{HS}}[\boldsymbol{t}](\boldsymbol{x}) := \int_S \boldsymbol{t}(\boldsymbol{y}) \cdot \boldsymbol{U}_{\mathrm{HS}}(\boldsymbol{x}, \boldsymbol{y}) \, \mathrm{d}S_y,$$

$$\mathcal{D}_{\mathrm{HS}}[\boldsymbol{u}](\boldsymbol{x}) := (\mathrm{P.V.}) \int_S \boldsymbol{u}(\boldsymbol{y}) \cdot \boldsymbol{T}_{\mathrm{HS}}(\boldsymbol{x}, \boldsymbol{y}) \, \mathrm{d}S_y \qquad (\boldsymbol{x} \in S) \qquad (18)$$

The overall size of the BE model is therefore much smaller than using the full-space Green's tensor (3) since the planar part Γ_0 of the free surface is no longer discretized (Fig. 2). The derivation and implementation of $\boldsymbol{U}_{\mathrm{HS}}, \boldsymbol{T}_{\mathrm{HS}}$ are however involved [64]. In particular, $\boldsymbol{U}_{\mathrm{HS}}$ and $\boldsymbol{T}_{\mathrm{HS}}$ cannot be expressed in the fashion of (3) in terms of simpler kernels having already-known multipole expansions, and a specific approach is needed.

4.1   Multipole expansions of the half-space Green's tensor

Complementary displacement Green's tensor.   The formulation of a multipole expansion for $\boldsymbol{U}_{\mathrm{HS}}$ has very recently been addressed in [18], and is now summarized for convenience. It exploits the additive decomposition

$$\boldsymbol{U}_{\mathrm{HS}}(\boldsymbol{x}, \boldsymbol{y}) = \boldsymbol{U}(\boldsymbol{x}, \boldsymbol{y}) + \widetilde{\boldsymbol{U}}(\boldsymbol{x}, \boldsymbol{y}) + \boldsymbol{U}_{\mathrm{C}}(\boldsymbol{x}, \boldsymbol{y}), \qquad (19)$$

where $\boldsymbol{U}$ is the full-space Green's tensor (3) and $\widetilde{\boldsymbol{U}}$ is the image full-space Green's tensor corresponding to an image point force $\boldsymbol{S} \cdot \boldsymbol{F}$ applied at the mirror image source point $\boldsymbol{S} \cdot \boldsymbol{x}$ (Fig. 3), i.e.

$$\widetilde{\boldsymbol{U}}(\boldsymbol{x}, \boldsymbol{y}) := \boldsymbol{U}(\boldsymbol{S} \cdot \boldsymbol{x}, \boldsymbol{y}) \cdot \boldsymbol{S}, \qquad (20)$$

with $\boldsymbol{S} := \boldsymbol{I} - 2\boldsymbol{e}_3 \otimes \boldsymbol{e}_3$ denoting the symmetry with respect to the free surface $y_3 = 0$. The complementary Green's tensor $\boldsymbol{U}_{\mathrm{C}}$ must then satisfy the homogeneous field equation and be such that $\boldsymbol{U}_{\mathrm{HS}}$ given by (19) satisfies the free-surface condition (15). A separated representation of $\boldsymbol{U}_{\mathrm{C}}$ was found [18] in the form of an inverse partial Fourier transform:

$$\boldsymbol{U}_{\mathrm{C}}(\boldsymbol{x}, \boldsymbol{y}) = \int_{\mathbb{R}^2} e^{\mathrm{i}(\xi_1 y_1 + \xi_2 y_2)} \, \hat{\boldsymbol{U}}_{\mathrm{C}}(\boldsymbol{\xi}, y_3; \boldsymbol{x}) \, \mathrm{d}\xi_1 \mathrm{d}\xi_2, \qquad (21)$$

where $\boldsymbol{\xi} := (\xi_1, \xi_2) \in \mathbb{R}^2$ are the transformed coordinates associated with (y_1, y_2) and with

$$\hat{\boldsymbol{U}}_{\mathrm{C}}(\boldsymbol{\xi}, y_3; \boldsymbol{x}) = \frac{1}{4\pi^2 \mu k_{\mathrm{S}}^2} \frac{s_{\mathrm{P}}(\xi)}{\delta(\xi)} \left[2\boldsymbol{V}_{\mathrm{S}}^+(\boldsymbol{\xi}) e^{s_{\mathrm{S}}(\xi)y_3} + \beta(\xi) \boldsymbol{V}_{\mathrm{P}}^+(\boldsymbol{\xi}) e^{s_{\mathrm{P}}(\xi)y_3} \right]$$
$$\otimes \left[2\boldsymbol{V}_{\mathrm{S}}^-(\boldsymbol{\xi}) \, e^{\boldsymbol{q}_{\mathrm{S}}^-(\boldsymbol{\xi}) \cdot \boldsymbol{x}} + \beta(\xi) \boldsymbol{V}_{\mathrm{P}}^-(\boldsymbol{\xi}) \, e^{\boldsymbol{q}_{\mathrm{P}}^-(\boldsymbol{\xi}) \cdot \boldsymbol{x}} \right]. \qquad (22)$$

In addition, the various scalar or vector functions appearing in (22) are defined by

$$\boldsymbol{q}_a^\pm(\boldsymbol{\xi}) = \pm \mathrm{i}\boldsymbol{\xi} + s_a(\xi)\boldsymbol{e}_3, \qquad s_a(\xi) = \sqrt{\xi^2 - k_a^2} \qquad (a = \mathrm{P,S}),$$

$$\beta(\xi) = k_{\mathrm{S}}^2 - 2\xi^2 = -(s_{\mathrm{S}}^2(\xi) + \xi^2), \qquad \delta(\xi) = \beta^2(\xi) - 4\xi^2 s_{\mathrm{P}}(\xi) s_{\mathrm{S}}(\xi),$$

$$\boldsymbol{V}_{\mathrm{S}}^\pm(\boldsymbol{\xi}) = \pm \left[s_{\mathrm{S}}(\xi) \, \boldsymbol{q}_{\mathrm{S}}^\pm(\boldsymbol{\xi}) + k_{\mathrm{S}}^2 \boldsymbol{e}_3 \right], \qquad \boldsymbol{V}_{\mathrm{P}}^\pm(\boldsymbol{\xi}) = \pm s_{\mathrm{P}}^{-1}(\xi) \boldsymbol{q}_{\mathrm{P}}^\pm(\boldsymbol{\xi})$$
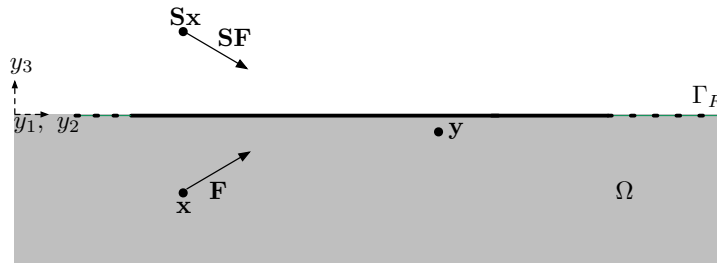

Figure 3: Image full-space Green's tensor: notations.

10

with $\xi := |\boldsymbol{\xi}| = (\xi_1^2 + \xi_2^2)^{1/2}$. Upon inserting (22) into (21), introducing polar coordinates in the Fourier space (i.e. setting $\boldsymbol{\xi} = (\xi_1, \xi_2) = \xi(\cos\alpha, \sin\alpha)$) and rearranging terms, the above formula can be recast in the following form:

$$\boldsymbol{U}_{\mathrm{C}}(\boldsymbol{x}, \boldsymbol{y}) = \frac{1}{4\pi^2 k_{\mathrm{S}}^2 \mu} \sum_{a,b=\mathrm{P,S}} \int_0^{+\infty} \xi s_{\mathrm{P}}(\xi) A_{ab}(\xi) \Bigg\{ \int_0^{2\pi} \big[\, \exp(\boldsymbol{q}_a^+(\xi,\alpha){\cdot}\boldsymbol{y})\, \boldsymbol{V}_a^+(\xi,\alpha)\,\big]$$
$$\otimes \big[\, \exp(\boldsymbol{q}_b^-(\xi,\alpha){\cdot}\boldsymbol{x})\, \boldsymbol{V}_b^-(\xi,\alpha)\,\big]\, \mathrm{d}\alpha \Bigg\}\, \mathrm{d}\xi. \quad (23)$$

with

$$A_{\mathrm{PP}}(\xi) := \frac{\beta^2(\xi)}{\delta(\xi)}, \quad A_{\mathrm{PS}}(\xi) = A_{\mathrm{SP}}(\xi) := \frac{2\beta(\xi)}{\delta(\xi)}, \quad A_{\mathrm{SS}}(\xi) := \frac{4}{\delta(\xi)}.$$

Decomposition (23) is separated, and has a structure reminiscent of the diagonal form (10).

Complementary traction Green's tensor. Most integral equations for semi-infinite media, such as (16), also require the complementary traction Green's tensor $\boldsymbol{T}_{\mathrm{C}}$, which is not addressed in [18]. To this aim, the complementary stress Green's tensor $\boldsymbol{\Sigma}_{\mathrm{C}} := \boldsymbol{\mathcal{C}} : \boldsymbol{\nabla}_y \boldsymbol{U}_{\mathrm{C}}$ is first derived by invoking Hooke's law (2) and noting that

$$\widehat{\boldsymbol{\nabla U}}_{\mathrm{C}}(\boldsymbol{\xi}, y_3; \boldsymbol{x}) = \mathrm{i}\boldsymbol{\xi} \otimes \hat{\boldsymbol{U}}_{\mathrm{C}}(\boldsymbol{\xi}, y_3; \boldsymbol{x}) + \boldsymbol{e}_3 \otimes \hat{\boldsymbol{U}}_{\mathrm{C}}'(\boldsymbol{\xi}, y_3; \boldsymbol{x}) \quad (24)$$

(with the prime ($'$) symbol denoting partial derivatives with respect to y_3) as a consequence of the partial Fourier representation (21) of $\boldsymbol{U}_{\mathrm{C}}$, to obtain

$$\hat{\boldsymbol{\Sigma}}_{\mathrm{C}}(\boldsymbol{\xi}, y_3; \boldsymbol{x}) = \mu(\kappa^{-2} - 2)\boldsymbol{I} \otimes \big[\mathrm{i}\boldsymbol{\xi}{\cdot}\hat{\boldsymbol{U}}(\boldsymbol{\xi}, y_3; \boldsymbol{x}) + \boldsymbol{e}_3{\cdot}\hat{\boldsymbol{U}}_{\mathrm{C}}'(\boldsymbol{\xi}, y_3; \boldsymbol{x})\big] + 2\mu\widehat{\boldsymbol{\nabla U}}_{\mathrm{C}}^{\mathrm{sym}}(\boldsymbol{\xi}, y_3; \boldsymbol{x})$$

(with κ defined by (4), and where "sym" indicates symmetrization with respect to the first two indices, noting that $\widehat{\boldsymbol{\nabla U}}$ is a third-order tensor). Substituting expression (22) into the above formula, performing straightforward derivations and rearranging terms, one arrives at the explicit formula

$$\hat{\boldsymbol{\Sigma}}_{\mathrm{C}}(\boldsymbol{\xi}, y_3; \boldsymbol{x}) = \frac{1}{4\pi^2 k_{\mathrm{S}}^2 \delta(\xi)} \Big(\beta(\xi) e^{s_{\mathrm{P}}(\xi)y_3} \big[2\boldsymbol{q}_{\mathrm{P}}^+(\boldsymbol{\xi}) \otimes \boldsymbol{q}_{\mathrm{P}}^+(\boldsymbol{\xi}) + (2\kappa^2 - 1)k_{\mathrm{S}}^2\boldsymbol{I}\big]$$
$$+ 2s_{\mathrm{P}}(\xi) e^{s_{\mathrm{S}}(\xi)y_3} \big[2s_{\mathrm{S}}(\xi)\, \boldsymbol{q}_{\mathrm{S}}^+(\boldsymbol{\xi}) \otimes \boldsymbol{q}_{\mathrm{S}}^+(\boldsymbol{\xi}) + k_{\mathrm{S}}^2\big(\boldsymbol{e}_3 \otimes \boldsymbol{q}_{\mathrm{S}}^+(\boldsymbol{\xi}) + \boldsymbol{q}_{\mathrm{S}}^+(\boldsymbol{\xi}) \otimes \boldsymbol{e}_3\big)\big]\Big)$$
$$\otimes \Big(2\boldsymbol{V}_{\mathrm{S}}^-(\boldsymbol{\xi})\, e^{\boldsymbol{q}_{\mathrm{S}}^-(\boldsymbol{\xi}){\cdot}\boldsymbol{x}} + \beta(\xi)\boldsymbol{V}_{\mathrm{P}}^-(\boldsymbol{\xi})\, e^{\boldsymbol{q}_{\mathrm{P}}^-(\boldsymbol{\xi}){\cdot}\boldsymbol{x}}\Big) \quad (25)$$

Finally, the traction Green's tensor $\boldsymbol{T}_{\mathrm{C}} := \boldsymbol{n}{\cdot}\boldsymbol{\Sigma}_{\mathrm{C}}$ for a given unit normal $\boldsymbol{n}$ is obtained in Fourier form as

$$\hat{\boldsymbol{T}}_{\mathrm{C}}(\boldsymbol{\xi}, y_3; \boldsymbol{x}) = \frac{1}{4\pi^2 k_{\mathrm{S}}^2 \delta(\xi)} \Big(2\boldsymbol{W}_{\mathrm{S}}(\boldsymbol{\xi}) e^{s_{\mathrm{S}}(\xi)y_3} + \beta(\xi)\boldsymbol{W}_{\mathrm{P}}(\boldsymbol{\xi}) e^{s_{\mathrm{P}}(\xi)y_3}\Big)$$
$$\otimes \Big(2\boldsymbol{V}_{\mathrm{S}}^-(\boldsymbol{\xi})\, e^{\boldsymbol{q}_{\mathrm{S}}^-(\boldsymbol{\xi}){\cdot}\boldsymbol{x}} + \beta(\xi)\boldsymbol{V}_{\mathrm{P}}^-(\boldsymbol{\xi})\, e^{\boldsymbol{q}_{\mathrm{P}}^-(\boldsymbol{\xi}){\cdot}\boldsymbol{x}}\Big) \quad (26)$$

with the vector functions $\boldsymbol{W}_{\mathrm{S}}$ and $\boldsymbol{W}_{\mathrm{P}}$ given by

$$\boldsymbol{W}_{\mathrm{S}}(\boldsymbol{\xi}) := s_{\mathrm{P}}(\xi)\big(\boldsymbol{q}_{\mathrm{S}}^+(\boldsymbol{\xi}){\cdot}\boldsymbol{n}\big)\big[2s_{\mathrm{S}}(\xi)\boldsymbol{q}_{\mathrm{S}}^+(\boldsymbol{\xi}) + k_{\mathrm{S}}^2\boldsymbol{e}_3\big] + k_{\mathrm{S}}^2 s_{\mathrm{P}}(\xi)(\boldsymbol{n}{\cdot}\boldsymbol{e}_3)\boldsymbol{q}_{\mathrm{S}}^+(\boldsymbol{\xi})$$
$$\boldsymbol{W}_{\mathrm{P}}(\boldsymbol{\xi}) := 2\big(\boldsymbol{q}_{\mathrm{S}}^+(\boldsymbol{\xi}){\cdot}\boldsymbol{n}\big)\boldsymbol{q}_{\mathrm{S}}^+(\boldsymbol{\xi}) + (2\kappa^2 - 1)k_{\mathrm{S}}^2\boldsymbol{n}$$

One notes the formal analogy between the partial Fourier expressions (22) of $\hat{\boldsymbol{U}}_{\mathrm{C}}$ and (26) of $\hat{\boldsymbol{T}}_{\mathrm{C}}$, the only difference lying in $\boldsymbol{V}_{\mathrm{S}}^+, \boldsymbol{V}_{\mathrm{P}}^+$ being replaced by $\boldsymbol{W}_{\mathrm{S}}, \boldsymbol{W}_{\mathrm{P}}$. Now, expressing

11

$\boldsymbol{T}_\mathrm{C}$ in terms of physical coordinates as the inverse partial Fourier transform (21) with $\hat{\boldsymbol{U}}_\mathrm{C}$ replaced by $\hat{\boldsymbol{T}}_\mathrm{C}$ and using polar coordinates in the Fourier space, one finally obtains

$$\boldsymbol{T}_\mathrm{C}(\boldsymbol{x}, \boldsymbol{y}) = \frac{1}{4\pi^2 k_\mathrm{S}^2} \sum_{a,b=\mathrm{P,S}} \int_0^{+\infty} \xi A_{ab}(\xi) \bigg\{ \int_0^{2\pi} \big[\exp(\boldsymbol{q}_a^+(\xi,\alpha)\cdot\boldsymbol{y})\, \boldsymbol{W}_a(\xi,\alpha) \big]$$
$$\otimes \big[\exp(\boldsymbol{q}_b^-(\xi,\alpha)\cdot\boldsymbol{x})\, \boldsymbol{V}_b^-(\xi,\alpha) \big] \mathrm{d}\alpha \bigg\} \mathrm{d}\xi. \quad (27)$$

with the $A_{ab}(\xi)$ again as defined for (23).

4.2   Fast multipole algorithm for the half-space Green's tensor

The single-layer and double-layer operators $\boldsymbol{\mathcal{S}}[\boldsymbol{t}]$, $\boldsymbol{\mathcal{D}}[\boldsymbol{u}]$ applied to given densities $\boldsymbol{t}$, $\boldsymbol{u}$ can then be, following (19) and using obvious notation, additively decomposed as

$$\boldsymbol{\mathcal{S}}_\mathrm{HS}[\boldsymbol{t}](\boldsymbol{x}) = \boldsymbol{\mathcal{S}}[\boldsymbol{t}](\boldsymbol{x}) + \widetilde{\boldsymbol{\mathcal{S}}}[\boldsymbol{t}](\boldsymbol{x}) + \boldsymbol{\mathcal{S}}_\mathrm{C}[\boldsymbol{t}](\boldsymbol{x}), \quad (28)$$
$$\boldsymbol{\mathcal{D}}_\mathrm{HS}[\boldsymbol{t}](\boldsymbol{x}) = \boldsymbol{\mathcal{D}}[\boldsymbol{t}](\boldsymbol{x}) + \widetilde{\boldsymbol{\mathcal{D}}}[\boldsymbol{t}](\boldsymbol{x}) + \boldsymbol{\mathcal{D}}_\mathrm{C}[\boldsymbol{t}](\boldsymbol{x}). \quad (29)$$

The contributions $\boldsymbol{\mathcal{S}}[\boldsymbol{t}](\boldsymbol{x})$, $\widetilde{\boldsymbol{\mathcal{S}}}[\boldsymbol{t}](\boldsymbol{x})$ and $\boldsymbol{\mathcal{D}}[\boldsymbol{u}](\boldsymbol{x})$, $\widetilde{\boldsymbol{\mathcal{D}}}[\boldsymbol{u}](\boldsymbol{x})$ are then evaluated using the standard diagonal-form FMM [19], whereas the complementary operators $\boldsymbol{\mathcal{S}}_\mathrm{C}$, $\boldsymbol{\mathcal{D}}_\mathrm{C}$ requires a specific treatment. Since the case of $\boldsymbol{\mathcal{S}}_\mathrm{C}$ is treated in detail in [18], attention is now focused on the computation of the complementary potential $\boldsymbol{\mathcal{D}}_\mathrm{C}[\boldsymbol{t}](\boldsymbol{x})$.

Substituting the representation (27) of $\boldsymbol{T}_\mathrm{C}$ into the definition of $\boldsymbol{\mathcal{D}}_\mathrm{C}[\boldsymbol{t}](\boldsymbol{x})$ and rearranging terms, the complementary double-layer operator is given by

$$\boldsymbol{\mathcal{D}}_\mathrm{C}[\boldsymbol{t}](\boldsymbol{x}) = \frac{1}{4\pi^2 k_\mathrm{S}^2} \sum_{a,b=\mathrm{P,S}} \int_0^{+\infty} \xi A_{ab}(\xi) \bigg\{ \int_0^{2\pi} \mathcal{R}_a^u(\xi,\alpha) \big[\exp(\boldsymbol{q}_b^-(\xi,\alpha)\cdot\boldsymbol{x})\, \boldsymbol{V}_b^-(\xi,\alpha) \big] \mathrm{d}\alpha \bigg\} \mathrm{d}\xi$$
$$(30)$$

where the multipole moments are given by

$$\mathcal{R}_a^t(\xi,\alpha) := \bigg\{ \int_S \exp(\boldsymbol{q}_a^+(\xi,\alpha)\cdot\boldsymbol{y})\, \boldsymbol{t}(\boldsymbol{y})\, \mathrm{d}S_y \bigg\} \cdot \boldsymbol{W}_a(\xi,\alpha). \quad (31)$$

Convergence of radial integral.   The radial integral in (30) is convergent whenever $x_3 + y_3 < 0$ due to the exponential decay of the integrand as $\xi \to +\infty$. On the other hand, noting that $\boldsymbol{W}_\mathrm{S} = O(\xi^4)$, $\boldsymbol{W}_\mathrm{P} = O(\xi^2)$, $\boldsymbol{V}_\mathrm{S}^- = O(\xi^2)$, $\boldsymbol{V}_\mathrm{P}^- = O(1)$, $\beta(\xi) = O(\xi^2)$ and $\delta(\xi) = O(\xi^2)$ (the latter estimate requiring straightforward derivations) for large ξ, the integrand of (30) is thus $O(\xi^5)$ if $x_3 + y_3 = 0$, making the radial integral divergent. The proposed acceleration approach is thus subject to the restriction $x_3 + y_3 < 0$, and is not applicable when $x_3 + y_3 = 0$ (i.e. for integration and collocation points both lying on Γ_F).

Clustering.   If convergent (i.e. whenever $x_3 + y_3 < 0$), integral (30) can be evaluated accurately, see next. In particular, unlike for more usual forms of the FMM, the representation (30) of $\boldsymbol{T}_\mathrm{C}$ is valid without requiring that clusters of source and collocation points be well-separated, making it unnecessary to subdivide the spatial region of interest into cells. The simplest option of applying (30) to all source and collocation points at once (i.e. of enclosing all points in one single cell) is permitted, and is used here.

Quadrature in Fourier space. The radial integration featured in (30) requires a quadrature rule that is suitable for a limited set of L integrals of the form

$$I_\ell(\boldsymbol{p}) = \int_0^{\xi_{\max}} f_\ell(\xi; \boldsymbol{p}) \, \mathrm{d}\xi \qquad (1 \le \ell \le L, \ \boldsymbol{p} \in \mathcal{P})$$

where $(f_\ell)_{1 \le \ell \le L}$ are real-valued square-integrable functions, whose (singular, oscillatory...) behavior may make numerical quadrature difficult (or *a priori* expensive). The f_ℓ are chosen so that all integrands appearing in (30) are linear combinations of them, while the parameters gathered in $\boldsymbol{p}$ are the frequency ω and the source and observation points $\boldsymbol{x}, \boldsymbol{y}$. The quadrature rule then must accurately evaluate all integrals $I_\ell(\boldsymbol{p})$ for all values of $\boldsymbol{p}$ in a given parameter domain $\mathcal{P}$, whose definition reflects the clusters of source and observation points used in $\boldsymbol{T}_{\mathrm{C}}(\boldsymbol{x}, \boldsymbol{y})$ and the frequencies of interest. To this aim, generalized Gaussian quadrature (GGQ) rules that are specific to the set of integrals $I_\ell(\boldsymbol{p})$ are computed by means of the GGQ generation methodology proposed in [14]. Its implementation for $\boldsymbol{U}_{\mathrm{C}}$ is described in detail in [18]; it is here adapted to the treatment of (30) by appropriately modifying the choice of input functions f_ℓ (the current treatment of (30) is based on $L = 38$ such functions, with a large number K of sampling values $\boldsymbol{p}_k \in \mathcal{P}$ used for each f_ℓ).

As a result, the Fourier integral (30) is evaluated by means of a product quadrature rule in (ξ, α)-space of the form

$$\boldsymbol{D}_{\mathrm{C}}[\boldsymbol{u}](\boldsymbol{x}) = \frac{1}{4\pi^2 k_{\mathrm{S}}^2} \sum_{a,b=\mathrm{P},\mathrm{S}} \sum_{i=1}^{n_\xi} w_i^\xi \xi_i A_{ab}(\xi_i)$$

$$\left\{ \sum_{j=1}^{n_\alpha} w_j^\alpha \mathcal{R}_a^u(\xi_i, \alpha_j) \left[\exp(\boldsymbol{q}_b^-(\xi_i, \alpha_j) \cdot \boldsymbol{x}) \, \boldsymbol{V}_b^-(\xi_i, \alpha_j) \right] \right\} + E(n_\xi, n_\alpha) \quad (32)$$

where $(\xi_i, w_i^\xi)_{1 \le i \le n_\xi}$ are the n_ξ GGQ nodes and weights for the radial integration, obtained by the procedure outlined above, $(\alpha_j, w_j^\alpha)_{1 \le j \le n_\alpha}$ are the n_α nodes and weights corresponding to a simple trapezoidal rule for the angular quadrature, and $E(n_\xi, n_\alpha)$ is the quadrature error. Finally, the simultaneous evaluation of both complementary operators $\boldsymbol{S}_{\mathrm{C}}[\boldsymbol{t}]$ and $\boldsymbol{D}_{\mathrm{C}}[\boldsymbol{u}]$ is decomposed into two steps: (i) computation of multipole moments $(a, b = \mathrm{P}, \mathrm{S})$

$$\mathcal{R}_a^t(\xi_i, \alpha_j) := \frac{1}{4\pi^2 k_{\mathrm{S}}^2 \mu} \left\{ \int_S \exp(\boldsymbol{q}_a^+(\xi_i, \alpha_j) \cdot \boldsymbol{y}) \, \boldsymbol{t}(\boldsymbol{y}) \, \mathrm{d}S_{\boldsymbol{y}} \right\} \cdot \boldsymbol{V}_a^+(\xi_i, \alpha_j)$$

$$\mathcal{R}_a^u(\xi_i, \alpha_j) := \frac{1}{4\pi^2 k_{\mathrm{S}}^2} \left\{ \int_S \exp(\boldsymbol{q}_a^+(\xi_i, \alpha_j) \cdot \boldsymbol{y}) \, \boldsymbol{u}(\boldsymbol{y}) \, \mathrm{d}S_{\boldsymbol{y}} \right\} \cdot \boldsymbol{W}_a(\xi_i, \alpha_j),$$

and (ii) operator evaluation at collocation points (quadrature in Fourier space)

$$\boldsymbol{S}_{\mathrm{C}}[\boldsymbol{t}](\boldsymbol{x}) = \sum_{a,b=\mathrm{P},\mathrm{S}} \sum_{i=1}^{n_\xi^t} w_i^t \xi_i^t A_{ab}(\xi_i^t) \left\{ \sum_{j=1}^{n_\alpha} w_j^\alpha \mathcal{R}_a^t(\xi_i^t, \alpha_j) \left[\exp(\boldsymbol{q}_b^-(\xi_i^t, \alpha_j) \cdot \boldsymbol{x}) \, \boldsymbol{V}_b^-(\xi_i^t, \alpha_j) \right] \right\}$$

$$\boldsymbol{D}_{\mathrm{C}}[\boldsymbol{u}](\boldsymbol{x}) = \sum_{a,b=\mathrm{P},\mathrm{S}} \sum_{i=1}^{n_\xi^u} w_i^u \xi_i^u B_{ab}(\xi_i^u) \left\{ \sum_{j=1}^{n_\alpha} w_j^\alpha \mathcal{R}_a^u(\xi_i^u, \alpha_j) \left[\exp(\boldsymbol{q}_b^-(\xi_i^u, \alpha_j) \cdot \boldsymbol{x}) \, \boldsymbol{V}_b^-(\xi_i^u, \alpha_j) \right] \right\}$$

Note that to minimize the overall quadrature work, separate GGQ rules $(\xi_i^t, w_i^t)_{1 \le i \le n_\xi^t}$ and $(\xi_i^u, w_i^u)_{1 \le i \le n_\xi^u}$ are generated and used for $\boldsymbol{S}_{\mathrm{C}}[\boldsymbol{t}]$ and $\boldsymbol{D}_{\mathrm{C}}[\boldsymbol{u}]$.

Extension to visco-elastodynamics. The extension of the FM-BEM for the elastic half-space Green's tensors to visco-elastodynamics is again done by introducing complex wavenumbers $k_\alpha^\star = k_\alpha(1 + \mathrm{i}\zeta_\alpha)$ ($\alpha = $ P,S), where $0 \le \zeta_\alpha \ll 1$ are the damping ratios. This modification does not affect the above methodology and results in any essential way. The only significant change caused by the switch to complex-valued wavenumbers consists in the redefinition of the collection of real-valued input functions that are used for generating the GGQ rule.

4.3 Accuracy of the elastodynamic half-space FMM

All the tests to follow assume material characteristics such that $\mu = 3$, $\rho = 1$ (in arbitrary units) and $\nu = 0.25$.

Accuracy of the radial quadrature. This first set of comparisons aims at checking the accuracy of the generalized Gaussian quadrature, a key component of the proposed treatment, for computing $\boldsymbol{T}_{\mathrm{HS}}$ in elastic or weakly dissipating media. For this purpose, the integral (27) is computed with the angular integration over α performed analytically (for this set of tests only) in order to focus on the accuracy of the GGQ for the radial quadrature, noting that (27) would in that case be exact were it not for the inability to perform analytically the radial integration. Due to the resulting lack of available exact reference values for $\boldsymbol{T}_{\mathrm{HS}}$, the numerical evaluations of $\boldsymbol{T}_{\mathrm{HS}}$ are compared to corresponding values $\boldsymbol{T}_{\mathrm{HS}}^{\mathrm{ref}}$ yielded by a non-multipole code (provided by B.B. Guzina [42]) which computes the viscoelastodynamic layered half-space Green's tensor using numerical evaluation of Bessel transforms. The contributions $\boldsymbol{T}$ and $\widetilde{\boldsymbol{T}}$ induced by the decomposition (19) of $\boldsymbol{T}_{\mathrm{HS}}$ are computed using the closed-form expression (3). The relative discrepancy on the (ijk) component of $\boldsymbol{\Sigma}_{\mathrm{HS}}$ is evaluated according to

$$\varepsilon_{ijk} = \frac{\|(\boldsymbol{\Sigma}_{\mathrm{HS}})_{ijk} - (\boldsymbol{\Sigma}_{\mathrm{HS}}^{\mathrm{ref}})_{ijk}\|_2}{\|(\boldsymbol{\Sigma}_{\mathrm{HS}}^{\mathrm{ref}})_{ijk}\|_2}. \tag{33}$$

While the GGQ rule was set to accurately evaluate $\boldsymbol{T}_{\mathrm{HS}}(\boldsymbol{x}, \boldsymbol{y})$ for all $(\boldsymbol{x}, \boldsymbol{y})$ such that $-4d \le y_1, y_2 \le 4d$ and $-4d \le y_3 \le -d$, the discrepancies (33) were evaluated for a source point at $\boldsymbol{x} = (2d, 3d, 2d)$ and observation points $\boldsymbol{y}$ on the line defined by $y_1 = 0.5d$, $y_2 = 0.75d$ and $-4d \le y_3 \le -d$, with the normalized frequency set to $k_{\mathrm{S}}d = 1/\sqrt{3}$. In Table 1, the relative discrepancies (33) on several components of $\boldsymbol{T}_{\mathrm{HS}}$ are shown for several sizes n_ξ of the GGQ rule and levels $\zeta_{\mathrm{P}} = \zeta_{\mathrm{S}} = \zeta$ of damping. As expected, the accuracy achieved on $\boldsymbol{T}_{\mathrm{HS}}$ increases with n_ξ; moreover, all the components have a similar level of accuracy, confirming the validity of using the same quadrature for all the components. Another useful observation is that the GGQ-based treatment works satisfactorily for purely elastic as well as weakly dissipative media, with the quadrature size n_ξ moreover seen to decrease when damping is present.

Moreover, the absolute accuracy of the quadrature rules produced by the GGQ generation algorithm can be assessed on a related situation for which exact reference values are available, namely that of the image full-space stress Green's tensor $\widetilde{\boldsymbol{\Sigma}}$ associated to (20). The resulting GGQ rule, generated under the same conditions (frequency, point clusters) as Table 1 and without damping ($\zeta_{\mathrm{P}} = \zeta_{\mathrm{S}} = 0$), is of size $n_\xi = 28$. The relative RMS errors on components of $\widetilde{\boldsymbol{\Sigma}}$, shown in Table 2, have magnitudes similar to the discrepancies given in Table 1 using the finest quadrature rule. This test thus confirms the reliability of the GGQ generation algorithm.

14

	n_ξ	ε_{111}	ε_{112}	ε_{113}	ε_{331}	ε_{333}
	39	$3.7\ 10^{-5}$	$1.1\ 10^{-4}$	$1.6\ 10^{-4}$	$3.4\ 10^{-4}$	$2.6\ 10^{-4}$
$\zeta = 0$	36	$1.2\ 10^{-4}$	$1.7\ 10^{-4}$	$7.8\ 10^{-4}$	$4.6\ 10^{-4}$	$5.4\ 10^{-4}$
	30	$7.3\ 10^{-4}$	$6.7\ 10^{-4}$	$7.6\ 10^{-3}$	$2.3\ 10^{-3}$	$4.2\ 10^{-3}$
	34	$9.3\ 10^{-5}$	$1.3\ 10^{-4}$	$7.7\ 10^{-4}$	$2.6\ 10^{-4}$	$5.4\ 10^{-4}$
$\zeta = 0.01$	30	$2.7\ 10^{-4}$	$2.7\ 10^{-4}$	$2.5\ 10^{-3}$	$8.4\ 10^{-4}$	$1.3\ 10^{-3}$
	27	$2.5\ 10^{-3}$	$2.5\ 10^{-3}$	$5.6\ 10^{-3}$	$7.6\ 10^{-3}$	$5.2\ 10^{-3}$
	33	$4.5\ 10^{-5}$	$1.1\ 10^{-4}$	$4.7\ 10^{-4}$	$3.0\ 10^{-4}$	$4.3\ 10^{-4}$
$\zeta = 0.05$	28	$4.4\ 10^{-4}$	$5.1\ 10^{-4}$	$3.0\ 10^{-3}$	$1.3\ 10^{-3}$	$1.7\ 10^{-3}$
	26	$1.7\ 10^{-3}$	$1.7\ 10^{-3}$	$1.1\ 10^{-2}$	$5.2\ 10^{-3}$	$5.8\ 10^{-3}$

Table 1: Relative discrepancy (33) on entries of the Green's tensor $\boldsymbol{\Sigma}_{\mathrm{HS}}$ for various values n_ξ of the radial quadrature rule density and for various levels $\zeta_{\mathrm{P}} = \zeta_{\mathrm{S}} = \zeta$ of damping ($k_{\mathrm{S}} d = 1/\sqrt{3}$).

n_ξ	ε_{111}	ε_{112}	ε_{113}	ε_{331}	ε_{333}
28	$1.9\ 10^{-5}$	$1.0\ 10^{-4}$	$8.1\ 10^{-5}$	$1.0\ 10^{-4}$	$7.7\ 10^{-5}$

Table 2: Relative discrepancy (33) on entries of the Green's tensor $\boldsymbol{\Sigma}_{\mathrm{FS}}$ for a GGQ rule with $n_\xi = 28$ points.

Example: scattering of an incident plane P wave by a spherical cavity in a half-space. To check the accuracy of this new FM-BEM based on the elastic half-space Green's tensors, the scattering of a vertical incident plane P wave by a spherical cavity bounded by the sphere S of radius r centered at $(0, 0, -3r)$, embedded in an elastic half-space $y_3 \leq 0$, is considered (Fig. 4). This problem may be formulated by means of either the integral equation for the total field $\boldsymbol{u}$

$$\mathcal{K}_{\mathrm{HS}}[\boldsymbol{u}](\boldsymbol{x}) = \boldsymbol{u}^F(\boldsymbol{x}) \quad (\boldsymbol{x} \in S) \tag{34}$$

based on the half-space Green's tensor, or the integral equation for the scattered field $\boldsymbol{u}^S := \boldsymbol{u} - \boldsymbol{u}^F$

$$\mathcal{K}[\boldsymbol{u}^S](\boldsymbol{x}) = -\boldsymbol{\mathcal{S}}[\boldsymbol{t}^F](\boldsymbol{x}) \quad (\boldsymbol{x} \in S \cup \Gamma_0) \tag{35}$$

based on the full-space Green's tensor and having set $\boldsymbol{t}^F = \boldsymbol{n} \cdot \boldsymbol{\mathcal{C}} : \boldsymbol{\nabla} \boldsymbol{u}^F$. Note that (34) results from the well-known expedient of applying the integral representation theorem to $\boldsymbol{u}^F$ inside S and combining the resulting identity with (16), and as a result involves only the double-layer integral operator $\boldsymbol{\mathcal{D}}_{\mathrm{HS}}$. Moreover, the given free field $\boldsymbol{u}^F$ is a known seismic wave in the reference half-space, here composed of the incident plane P wave and the wave reflected by the free surface Γ_F.

Results from FM-BEM formulations based on either (34) or (35) are compared in Fig. 5. Formulation (35) required the meshing of a disk-shaped truncated free surface $\Gamma_0(D)$ (Fig. 4a), with the truncation radius set to $D = 5r$, while formulation (34) needed only a mesh of the cavity surface S (Fig. 4b). Enforcing a uniform, and identical, mesh density in both formulations (here set to 10 BE nodes per S wavelength), the number of DOFs for the full-space BIE formulation (N_{FS}) and the half-space BIE formulation (N_{HS}) are such that $N_{\mathrm{FS}} \approx 7.25 N_{\mathrm{HS}}$. The non-dimensional frequency used was $k_{\mathrm{S}} r = 2.5\pi$, leading respectively to $N_{\mathrm{FS}} = 38{,}934$ and $N_{\mathrm{HS}} = 7{,}686$. The total displacement computed on S using the two approaches coincide within a relative discrepancy of about 10^{-3}.

15

(a) Using full-space Green's tensors (Eq. (35)).
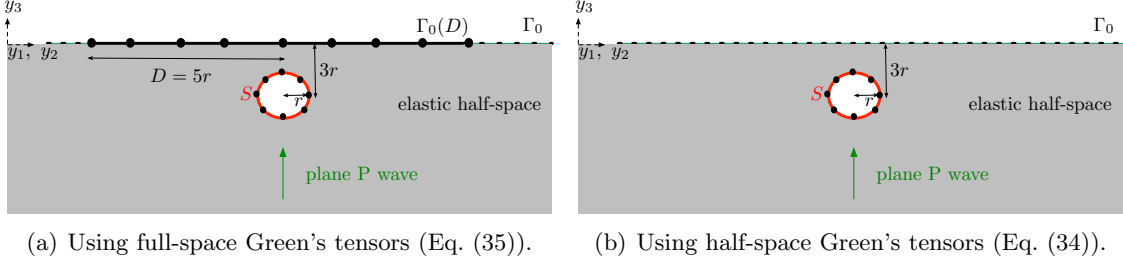
(b) Using half-space Green's tensors (Eq. (34)).

Figure 4: Scattering of a vertical incident plane P wave by a spherical cavity in an elastic half-space. In case (a), the BE mesh includes the artificially truncated free surface $\Gamma_0(D)$.
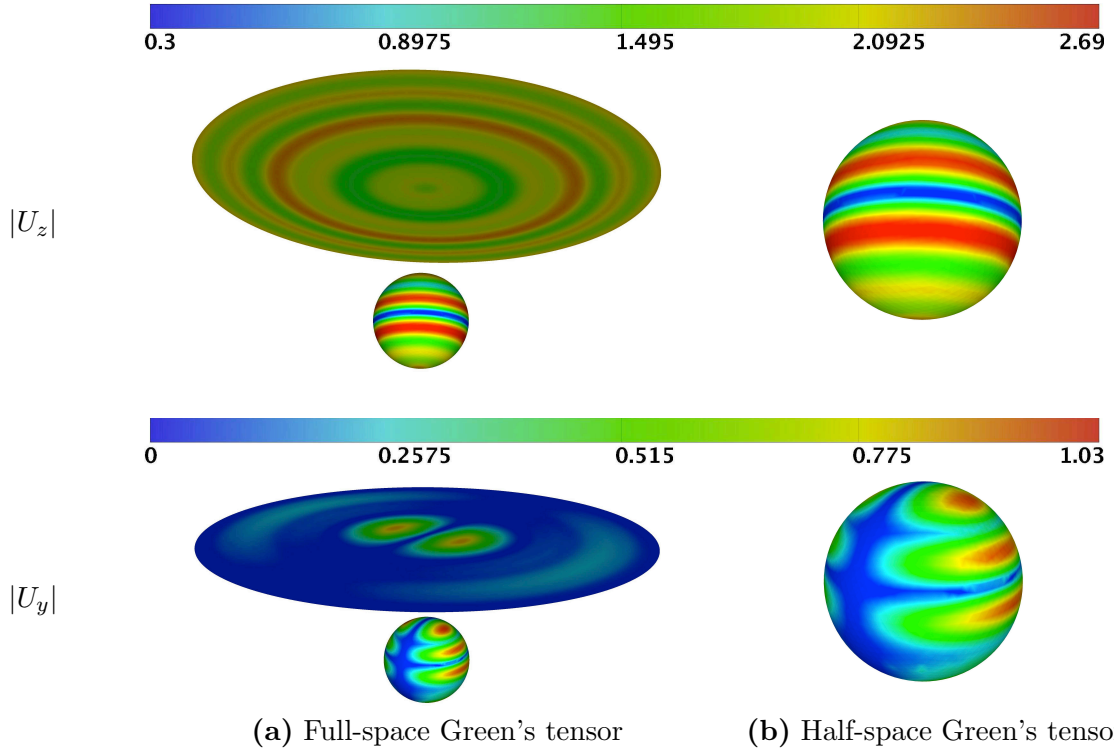

(a) Full-space Green's tensor

(b) Half-space Green's tensor

Figure 5: Comparison of the vertical and horizontal modulus of displacement obtained with (a) the full-space formulation (35) and (b) the half-space formulation (34).

Remarks on computational complexity. The computational complexities of the full-space and half-space formulations are different. The former is known to be $\mathcal{O}(N_{FS}\log N_{FS})$. The latter is $\mathcal{O}(N_{HS}n_\xi n_\alpha)$, where the GGQ size (n_ξ, n_α) cannot easily be evaluated by analytical means as (i) it is obtained using a numerical algorithm, and (ii) it depends on preset accuracy level, frequency, and on the size and depth of clusters of points $\boldsymbol{x}, \boldsymbol{y}$ (with the radial size n_ξ increasing as clusters of points $\boldsymbol{x}, \boldsymbol{y}$ are closer to Γ_F). The half-space FMM complexity is estimated in [18], using numerical experiments and for single-layer potentials, to be $\approx \mathcal{O}(N^{1.5})$ for clusters of points at shallow depth. This matter requires substantial additional investigation.

5 Ongoing work and directions for future work

Directions for future work that aims at building on the encouraging results already achieved by the 3D visco-elastodynamic FM-BEM and expanding its scope and capabilities are now discussed, with pointers to relevant published material given in the process.

Preconditioning. Many studies, including [19, 20] for elastodynamics, have shown that the GMRES iteration count can significantly hinder the overall efficiency of the FM-BEM, especially for multi-region configurations. Preconditioning the FM-BEM is therefore an important practical issue. A natural candidate for the preconditioning matrix is the (sparse) matrix $\mathbf{K}^{\text{near}}$ gathering the contributions to $\mathbf{K}$ arising from adjacent cells. For example, a simple preconditioning approach, based on an inner-outer GMRES algorithm where the preconditioning system $\mathbf{K}^{\text{near}}\mathbf{w}^{(k+1)} = \mathbf{K}\mathbf{w}^{(k)}$ yielding the $k + 1$-th Krylov vector $\mathbf{w}^{(k+1)}$ (with $\mathbf{w}^{(k)}$ known) is solved using a low-accuracy GMRES, was found in [21] to improve the computational performance, with analysis running times roughly halved. Numerical tests included a seismological configuration, namely the propagation of seismic waves in an alpine basin (Grenoble, France).

The inner-outer GMRES approach, while usefully improving performance and being simple to implement, suffers from the fact that the iteration count still grows with the problem size and frequency and thus remains a major limiting factor. Other approaches for preconditioning the FM-BEM have been considered. A two-level iterative approach, where the Krylov vector computed at each iteration of the main GMRES solver is obtained by solving a low-accuracy FMM used as preconditioner, has been proposed in [17] for electromagnetic problems. Other, more traditional, preconditioning approaches such as incomplete LU, SParse Approximative Inverse [17], multi-grid methods [16] have also been applied to electromagnetic FM-BEMs. All these approaches are algebraic in nature. Since the FMM allows to assemble a small part of the complete influence matrix $\mathbf{K}$ (e.g. $\mathbf{K}^{\text{near}}$) but not $\mathbf{K}$ in full, insufficient information is available for the definition of an efficient algebraic preconditioner. Algebraic approaches are hence inherently limited in the performance improvement they can deliver, as is witnessed by the various studies done for electromagnetic FM-BEMs, and the same conclusion is expected for elastodynamics.

A completely different approach to FM-BEM preconditioning, analytic in nature, consists in exploiting mathematical properties of the relevant continuous integral operators. It is so far less developed and more intrusive in terms of coding. In particular, preconditioners based on the Calderón identities verified by the integral operators, have produced good results, for both the standard BEM and the FM-BEM. Calderón analytic preconditioners have for example been proposed for the Laplace equation [74], the Helmholtz equation [23], non-periodic problems for 2D Helmholtz [4] and periodic FMMs for 3D elastodynamics [46]. Other strategies have been proposed in electromagnetism to reformulate the integral operator, at the continuous level, to obtain well-conditioned formulations. For example in [3, 5, 15] the boundary integral operator is forced to be a compact perturbation of the identity operator. Darbas *et al.* [27] present the successful combination of an On-Surface Radiation Condition (OSRC)-based preconditioner and a FM-BEM to define an efficient solver for 3-D acoustic scattering by sound-hard obstacles at high frequencies. The main advantages of this preconditioner are its simple implementation and its very low additional computational cost. Most importantly, this approach is found to be much more efficient than algebraic preconditioners as numerical experiments show the iteration count to be essentially independent on both the frequency and the problem size [27]. OSRC-based

preconditioners are expected to be equally suitable for for elastodynamic FM-BEMs. They will be developed in future work, a task that requires substantial preparatory mathematical work in view of the higher complexity of elastodynamic integral operators.

Direct solvers for fast BEMs. Fast BEMs have been so far primarily developed in conjunction with iterative solvers. The latter however still suffer from limitations caused by the growth of the condition number of $\mathbf{K}$ with N or ω. This has motivated recent interest in fast direct solvers that are applicable to large-scale BE models. Indeed, direct solvers are robust and lead to solution times that do not depend on the condition number. Moreover, they allow to deal efficiently with multiple right-hand sides, which is very useful in e.g. parametric studies. Methods proposed so far for solving (8) directly rely on the rank-deficient character of the off-diagonal blocks (a property also implicitly used by the FMM). In [72], the ACA is used for accelerating the LU factorization of the system arising from a frequency-domain BEM for the Maxwell equations. Another approach, based on a data-sparse hierarchical factorization, is proposed in [43, 57] for Laplace or low-frequency Helmholtz equations. Even though the solver efficiency is found to deteriorate for oscillatory kernels, the method remains competitive for objects of characteristic size less than about two hundred wavelengths. To the present authors' best knowledge, similar approaches have not yet been tried for 3D elastodynamics, and certainly deserve investigation in that context.

Parallelization. In [18–20], the implementation of the elastodynamic FM-BEM has been done for single-processor platforms. While that form of the FM-BEM has been shown to already perform considerably better than the standard BEM, its parallelization will further extend its capabilities in terms of e.g. BEM model size or frequency range.

The parallelization of the FMM is a timely issue, as witnessed e.g. by the 2010 Gordon Bell Prize (rewarding outstanding achievement in high-performance computing) awarded to the team led by G. Biros for its work on the simulation of red blood cells with the FMM [52]. They created a blood-flow simulation of 260 million deformable red blood cells flowing in plasma (corresponding to 90 billion unknown DOFs). To achieve such performance, the kernel-independent FMM [30] was massively parallelized to accelerate the long-range hydrodynamic interactions between cells and plasma.

The parallelization of the FMM is not an easy task. A natural idea is to associate an octree cell to a single processor. However, various stages of the algorithm (near contributions, upward and downward passes, transfers) link at least two cells. As a result, it is important to assign the cells to the processors so as to minimize communication time between processors. This issue has been studied, for real-world applications of FMM-based solvers for Maxwell's equations, in [17, 76, 78]. Seismology-oriented applications of the visco-elastodynamic FM-BEM will also require parallelization in order to be applicable to the frequencies and complex geometrical configurations of interest.

Computation of transient responses. The time-domain BEM involves convolution integrals with respect to time. Such convolutions can be computed directly in the time domain by using time-domain fundamental solutions. The stability in time of transient BIE formulations is however known to be very sensitive to the choice of the time step [36]. Even though a stable formulation, stemming from an energy-based variational principle, is known for the wave equation [2], the derivation and implementation of a transient FMM is

not easy (see e.g. the 3D transient elastodynamic fast BEM formulation of [79], where the required separated decomposition of the space-time kernels is achieved by means of plane wave expansion).

An alternative approach is to solve the problem via a frequency-domain BEM and then apply a Fourier transform to synthesize the results in the time domain. The solution of the time-dependent problem is turned into the solution of a sequence of independent frequency-domain problems. In [20], time-domain results have been obtained via frequency-domain analyses at sampling frequencies and a Fourier transform. However this method is known to suffer from instabilities related to the choice of the sampling parameters.

Another promising avenue, which is intermediate between a direct time-domain approach and a frequency-time domain approach is to use the Convolution Quadrature Method (CQM) [56] for developing a time-stepping scheme in conjunction with the Laplace-transformed fundamental solution. This approach avoids highly technical implementation work required by, and stability issues arising with, time-domain BIEs based on retarded potentials. It also allows to re-use known kernel decompositions in the Laplace domain and to easily accommodate visco-elastic behavior. CQM-based transient BEMs have been successfully developed for 3D elastodynamics [49], viscoelasticity [69] and wave problems [8]. The CQM is also used in the fast ACA-based BEM for elastodynamics of [58] and in conjunction with the FMM for scalar wave problems in [67]. To the authors best knowledge, no CQM-based FM-BEM elastodynamic formulation has yet been proposed.

Coupling with other numerical methods. Except for a few, very specific types of heterogeneity for which fundamental solutions are explicitly known, BIE formulations are restricted to piecewise-homogeneous media, an assumption which is often inadequate at least for near-field modelling purposes. A natural approach then consists in coupling domain discretization methods such as the FEM, which has the necessary flexibility for dealing with non-homogeneous or non-linear materials, with the FM-BEM, which efficiently handles unbounded media with simple properties, an assumption which is usually acceptable for long-range modelling. This approach allows to avoid large domain meshes and artificial-truncation issues, and as such can be viewed as an alternative approach to standard absorbing boundary conditions (ABCs). Perfectly matched layers (PMLs) and the high-order ABCs rely on, and are sensitivity to, algorithmic parameters such as the thickness of the layer for PMLs, whereas the FM-BEM/FEM is not expected to critically rely on specific parameters.

In a recent study in the context of dynamic soil-structure interaction, Coulier *et al.* [25] compare three methods for coupling the ACA-accelerated BEM to the FEM: (i) a classical direct coupling [48] (where the FE and BE domains are assembled into a single matrix equation to which a direct solver is applied), (ii) an iterative coupling (where the FE and BE equations are solved independently but the boundary conditions are updated at each iteration) and (iii) a monolithic coupling (where the BE and FE equations are solved simultaneously as strong fluid-structure coupling [44]). Option (i) is found to be the least efficient, the relative performance of (ii) and (iii) being strongly application-dependent. A preliminary, and incomplete, study on the coupling of elastodynamic FM-BEM with the FEM is proposed in the recent thesis [38], where a sequential Dirichlet-Neumann coupling (which is a kind of iterative coupling) and a simultaneous coupling (using an implicit condensation approach for the FE contribution to the system [35]) are compared.

19

A posteriori error estimate and adaptive mesh refinement. So far, most of the effort has been dedicated to the acceleration of the solution of the boundary integral equation. To address real-life computational problems, it is also necessary to develop tools for guaranteeing a prescribed level of solution accuracy. Moreover, adaptive meshing procedures also allow to reduce CPU time, since an optimal mesh will minimize the problem size N necessary for achieving a desired level of accuracy. Employing sequences of adapted meshes can also be considered as a simple non-intrusive way to reduce the number of iterations used by the linear solver. Since the iteration count increases with N, one may start from a coarse mesh, for which the iteration count is expected to be small, followed by increasingly refined and adapted meshes with the initial guess for each mesh set to the solution obtained with the previous mesh. The number of iterations required for each refinement level is expected to be stable, and the total CPU time to be competitive with solving the problem directly on a fine enough mesh with an algebraic preconditioner.

The development of a posteriori error estimation methodologies, while being essential for reliable and efficient computations, is at a less advanced stage for the BEMs than for the FEMs. Significant advances on error estimation for Galerkin BEM formulations of 3D Laplace problems have been recently made in the group of D. Praetorius [33]. The most challenging aspect of error estimation for BEMs is its potentially high computational cost caused by the non-local character of integral operators.

Regarding the collocation BEM approach, which is up to now often used in elastodynamic (FM)-BEM implementations, the main error estimation strategies are of two types [50], namely the residual type (using the value of the integral equation residual as an error estimate) and the interpolation error type (using higher interpolation order in the shape functions). Since, by definition, the BIE residual is forced to be zero at collocation points, techniques specific to collocation BEM have been proposed. Other error estimation methods proposed for the Galerkin BEM or for FEMs can also be extended to the collocation BEM.

The aforementioned error estimation methods have been proposed for standard BEM, and have not so far been tested on large-scale problems due to the usual limitations of non-accelerated BEMs. An extensive study of the behavior of error estimates applied to FM-BEMs is needed. An additional motivation for such an investigation lies in the possibility of defining efficient stopping criteria for iterative solvers, by comparing the discretization and algebraic error estimates; this approach has been studied in [47] for elliptic problems solved by the FEM.

References

[1] Achenbach, J. D. *Wave Propagation in Elastic Solids*. North-Holland (1984).

[2] Aimi, A., Diligenti, M., Guardasoni, C., Mazzieri, I., Panizzi, S. An energy approach to space–time Galerkin BEM for wave propagation problems. *Int. J. Num. Meth. Eng.*, **80**:1196–1240 (2009).

[3] Alouges, F., Borel, S., Levadoux, D. P. A stable well-conditioned integral equation for electromagnetism scattering. *J. Comp. Appl. Math.*, **204**:440–451 (2007).

[4] Antoine, X., Boubendir, Y. An integral preconditioner for solving the two-dimensional scattering transmission problem using integral equations. *Int. J. Computer Math.*, **85**:1473–1490 (2008).

[5] Antoine, X., Darbas, M. Alternative integral equations for the iterative solution of acoustic scattering problems. *Quart. J. Mech. Appl. Math.*, **58**:107–128 (2005).

[6] Arias, I., Achenbach, J. D. Rayleigh wave correction for the BEM analysis of two-dimensional elastodynamic problems in a half-space. *Int. J. Num. Meth. Eng.*, **60**:2131–2146 (2004).

[7] Baffet, D., Bielak, J., Givoli, D., Hagstrom, T., Rabinovich, D. Long-time stable high-order absorbing boundary conditions for elastodynamics. *Comp. Meth. Appl. Mech. Eng.*, **241-244**:20–37 (2012).

[8] Banjai, L., Schanz, M. *Wave propagation problems treated with convolution quadrature and BEM*, pp. 145–184. Springer (2012).

[9] Bebendorf, M. *Hierarchical matrices: a means to efficiently solve elliptic boundary value problems*, vol. 63 of *Lecture Notes in Computational Science and Engineering*. Springer (2008).

[10] Bebendorf, M., Grzhibovskis, R. Accelerating Galerkin BEM for linear elasticity using adaptive cross approximation. *Math. Meth. Appl. Sci.*, **29**:1721–1747 (2006).

[11] Beer, G., Smith, I., Duenser, C. *The boundary element method with programming*. Springer (2008).

[12] Beskos, D. E. Boundary element methods in dynamic analysis, part. II (1986–1996). *Appl. Mech. Rev.*, **50**:149–197 (1997).

[13] Bonnet, M. *Boundary Integral Equation Method for Solids and Fluids*. John Wiley and Sons (1999).

[14] Bremer, J., Gimbutas, Z., Rokhlin, V. A nonlinear optimization procedure for generalized gaussian quadrature. *SIAM J. Sci. Comp.*, **32**:1761–1788 (2010).

[15] Bruno, O., Elling, T., Turc, C. Regularized integral equations and fast high-order solvers for sound-hard acoustic scattering problems. *Int. J. Numer. Meth. Eng.*, **91**:1045–1072 (2012).

[16] Carpentieri, B. A matrix-free two-grid preconditioner for solving Boundary Integral Equations in Electromagnetism. *Computing*, **77**:275–296 (2006).

[17] Carpentieri, B., Duff, I. S., Giraud, L., Sylvand, G. Combining fast multipole techniques and an approximate inverse preconditioner for large parallel electromagnetics calculations. *SIAM J. Sci. Comp.*, **27**:774–792 (2005).

[18] Chaillat, S., Bonnet, M. A new Fast Multipole Formulation for the elastodynamic half-space Green's tensor. *Under review* (2013).

[19] Chaillat, S., Bonnet, M., Semblat, J. F. A multi-level fast multipole BEM for 3-D elastodynamics in the frequency domain. *Comp. Meth. Appl. Mech. Eng.*, **197**:4233–4249 (2008).

[20] Chaillat, S., Bonnet, M., Semblat, J. F. A new fast multi-domain BEM to model seismic wave propagation and amplification in 3D geological structures. *Geophys. J. Int.*, **177**:509–531 (2009).

[21] Chaillat, S., Semblat, J.F ., Bonnet, M. A preconditioned 3-D multi-region fast multipole solver for seismic wave propagation in complex geometries. *Commun. Comp. Phys.*, **11**:594–609 (2012).

[22] Cheng, H., Crutchfield, W. Y., Gimbutas, Z., Greengard, L. F., Ethridge, J. F., Huang, J., Rokhlin, V., Yarvin, N., Zhao, J. A wideband fast multipole method for the Helmholtz equation in three dimensions. *J. Comp. Phys.*, **216**:300–325 (2006).

[23] Christiansen, S. H., Nédélec, J. C. A preconditioner for the electric field integral equation based on Calderón formulas. *SIAM J. Num. Anal.*, **40**:1100–1135 (2002).

[24] Clouteau, D., Cottereau, R., Lombaert, G. Dynamics of structures coupled with elastic media — A review of numerical models and methods. *J. Sound Vibr.*, p. in press (2012).

[25] Coulier, P., François, S., Lombaert, G., Degrande, G. A coupled finite element-hierarchical boundary element method based on Green's functions for a horizontally layered half-space. In N. Heuer, C. Jerez-Hanckes (eds.), *Proceedings of the IABEM Symposium (Santiago, Chile)*, pp. 23–30 (2013).

[26] Cruse, T. A., Rizzo, F. J. A direct formulation and numerical solution of the general transient elastodynamic problem. I. *J. Math. Anal. Appl.*, **22**:244–259 (1968).

[27] Darbas, M., Darrigrand, E., Lafranche, Y. Combining analytic preconditioner and Fast Multipole Method for the 3D Helmholtz equation. *J. Comp. Phys.* (to appear).

[28] Darve, E. The fast multipole method: I. Error analysis and asymptotic complexity. *SIAM J. Numer. Anal.*, **38**:98–128 (2000).

[29] Darve, E. The Fast Multipole Method: Numerical Implementation. *J. Comp. Phys.*, **160**:195–240 (2000).

[30] Engquist, B., Ying, L. Fast directional multilevel algorithms for oscillatory kernels. *SIAM J. Sci. Comp.*, **29**:1710–1737 (2007).

[31] Epton, M.A., Dembart, B. Multipole translation theory for the three-dimensional Laplace and Helmholtz equations. *SIAM J. Sci. Comp.*, **16**:865–897 (1995).

[32] Eringen, A. C., Suhubi, E. S. *Elastodynamics, Vol. II-Linear Theory.*. Academic Press (1975).

[33] Feischl, M., Karkulik, M., Melenk, J., Praetorius, D. Quasi-optimal convergence rate for an adaptive boundary element method. *SIAM J. Numer. Anal.* (2013, in press).

[34] Fong, W., Darve, E. The black-box fast multipole method. *J. Comp. Phys.*, **228**:8712–8725 (2009).

[35] Frangi, A., Ghezzi, L., Faure-Ragani, P. Accurate force evaluation for industrial magnetostatics applications with fast BEM-FEM approaches. *Comp. Model. Eng. Sci.*, **15**:41–48 (2006).

[36] Frangi, A., Novati, G. On the numerical stability of time-domain elastodynamic analyses by BEM. *Comp. Meth. Appl. Mech. Eng.*, **173**:403–417 (1999).

[37] Fujiwara, H. The fast multipole method for solving integral equations of three-dimensional topography and basin problems. *Geophys. J. Int.*, **140**:198–210 (2000).

[38] Grasso, E. *Modelling visco-elastic seismic wave propagation : a fast-multipole boundary element method and its coupling with finite elements*. Ph.D. thesis, Université Paris-Est (2012). http://tel.archives-ouvertes.fr/tel-00730752.

[39] Grasso, E., Chaillat, S., Bonnet, M., Semblat, J.F. Application of the multi-level time-harmonic fast multipole BEM to 3-D visco-elastodynamics. *Eng. Anal. Bound. Elem.*, **36**:744–758 (2012).

[40] Greengard, L., Huang, J. F., Rokhlin, V., Wandzura, S. Accelerating fast multipole methods for the Helmholtz equation at low frequencies. *IEEE Comput. Sci. Eng.*, **5**:32–38 (1998).

[41] Greengard, L., Rokhlin, V. A fast algorithm for particle simulations. *J. Comp. Phys.*, **73**:325–348 (1987).

[42] Guzina, B. B., Pak, R. Y. S. On the Analysis of Wave Motions in a Multi-Layered Solid. *Quart. J. Mech. Appl. Math.*, **54**:13–37 (2001).

[43] Ho, K.L., Greengard, L. A fast direct solver for structured linear systems by recursive skeletonization. *SIAM J. Sci. Comp.*, **34**(5):2507–2532 (2012).

[44] Hübner, B., Walhorn, E., Dinkler, D. A monolithic approach to fluid–structure interaction using space–time finite elements. *Comp. Meth. Appl. Mech. Eng.*, **193**:2087–2104 (2004).

[45] Ihlenburg, F., Babuška, I. Dispersion analysis and error estimation of Galerkin finite element methods for the Helmholtz equation. *Int. J. Numer. Meth. Engng.*, **38**:3745–3774 (1995).

[46] Isakari, H., Niino, K., Yoshikawa, H., Nishimura, N. Calderon's preconditioning for periodic fast multipole method for elastodynamics in 3D. *Int. J. Num. Meth. Eng.*, **90**:484–505 (2012).

[47] Jiránek, P., Strakoš, Z., Vohralík, M. A posteriori error estimates including algebraic error and stopping criteria for iterative solvers. *SIAM J. Sci. Comp.*, **32**:1567–1590 (2010).

[48] Kausel, E., Roësset, J.M. Stiffness matrices for layered soils. *Bull. seism. Soc. Am.*, **71**:1743–1761 (1981).

[49] Kielhorn, L., Schanz, M. Convolution quadrature method-based symmetric Galerkin boundary element method for 3-D elastodynamics. *Int. J. Num. Meth. Eng.*, **76**:1724–1746 (2008).

[50] Kita, E., Kamiya, N. Error estimation and adaptive mesh refinement in boundary element method, an overview. *Eng. Anal. Bound. Elem.*, **25**:479–495 (2001).

[51] Kupradze, V. D., Gegelia, T.G. *Dynamical problems in elasticity*. Progress in solid mechanics, vol. III, North Holland (1963).

[52] Lashuk, I., Chandramowlishwaran, A., Langston, H., Nguyen, T.A., Sampath, R., Shringarpure, A., Vuduc, R., Ying, L., Zorin, D., Biros, G. A massively parallel adaptive fast multipole method on heterogeneous architectures. *Commun. ACM*, **55**:101–109 (2012).

[53] Liu, Y., Nishimura, N., Otani, Y., Takahashi, T., Chen, X. L., Munakata, H. A fast boundary element method for the analysis of fiber-reinforced composites based on a rigid-inclusion model. *ASME J. Appl. Mech.*, **72**:115–128 (2005).

[54] Liu, Y. J., Mukherjee, S., Nishimura, N., Schanz, M., Ye, W., Sutradhar, A., Pan, E., Dumont, N. A., Frangi, A., Saez, A. Recent Advances and Emerging Applications of the Boundary Element Method. *Appl. Mech. Rev.*, **64**:030802 (2011).

[55] Lu, C.C, Chew, W.C. Fast algorithm for solving hybrid integral equations. *Microwaves, Antennas and Propagation, IEE Proc. H*, **140**:455–460 (1993).

[56] Lubich, C. Convolution quadrature and discretized operational calculus. I. *Numerische Mathematik*, **52**:129–145 (1988).

[57] Martinsson, P.G., Rokhlin, V. A fast direct solver for scattering problems involving elongated structures. *J. Comp. Phys.*, **221**(1):288–302 (2007).

[58] Messner, M., Schanz, M. An accelerated symmetric time-domain boundary element formulation for elasticity. *Eng. Anal. Bound. Elem.*, **34**:944–955 (2010).

[59] Messner, M., Schanz, M., Darve, E. Fast directional multilevel summation for oscillatory kernels based on Chebyshev interpolation. *J. Comp. Phys.*, **231**:1175–1196 (2012).

[60] Milazzo, A., Benedetti, I., Aliabadi, M. H. Hierarchical fast BEM for anisotropic time-harmonic 3-D elastodynamics. *Comp. Struct.*, **96-97**:9–24 (2012).

[61] Nédélec, J. C. *Acoustic and electromagnetic equations*. Applied mathematical sciences (vol. 144). Springer (2001).

[62] Nishimura, N. Fast multipole accelerated boundary integral equation methods. *Appl. Mech. Reviews*, **55**:299–324 (2002).

[63] Pak, R.Y.S., Guzina, B. B. Seismic soil-structure interaction analysis by direct boundary element methods. *Int. J. Solids Struct.*, **36**:4743–4766 (1999).

[64] Pan, L., Rizzo, F., Martin, P.A. Some efficient boundary integral strategies for time-harmonic wave problems in an elastic halfspace. *Comp. Meth. Appl. Mech. Eng.*, **164**:207–221 (1998).

[65] Rokhlin, V. Rapid solution of integral equations of classical potential theory. *J. Comp. Phys.*, **60**:187–207 (1985).

[66] Saad, Y., Schultz, M. H. GMRES: a Generalized Minimal Residual Algorithm for solving nonsymmetric linear systems. *SIAM J. Sci. Comp.*, **7**:856–869 (1986).

[67] Saitoh, T., Hirose, S. Parallelized fast multipole BEM based on the convolution quadrature method for 3-D wave propagation problems in time-domain. *IOP Conference Series: Materials Science and Engineering*, **10**:012242 (2010).

[68] Sakuma, T., Yasuda, Y. Fast multipole boundary element method for large-scale steady-state sound field analysis. Part I: setup and validation. *Acta Acustica united with Acustica*, **88**:513–525 (2002).

[69] Schanz, M. A boundary element formulation in time domain for viscoelastic solids. *Comm. Numer. Meth. Eng.*, **15**:799–809 (1999).

[70] Schneider, S. FE/FMBE coupling to model fluid–structure interaction. *Int. J. Num. Meth. Eng.*, **76**:2137–2156 (2008).

[71] Semblat, J. F. Modeling Seismic Wave Propagation and Amplification in 1D/2D/3D Linear and Nonlinear Unbounded Media. *ASCE Int. J. Geomech.*, **11**:440–448 (2011).

[72] Shaeffer, J. Direct solve of electrically large integral equations for problem sizes to 1 M unknowns. *IEEE Trans. Antennas Propag.*, **56**(8):2306–2313 (2008).

[73] Song, J. M., Chew, W. C. Multilevel fast-multipole algorithm for solving combined field integral equations of electromagnetic scattering. *Microw. Opt. Technol. Lett.*, **10**:14–19 (1995).

[74] Steinbach, O., Wendland, W.L. The construction of some efficient preconditioners in the boundary element method. *Adv. Comp. Math.*, **9**:191–216 (1998).

[75] Sylvand, G. *La méthode multipôle rapide en éléctromagnétisme : performances, parallélisation, applications*. Ph.D. thesis, ENPC (2002). http://bib.rilk.com/308/.

[76] Sylvand, G. Performance of a parallel implementation of the FMM for electromagnetics applications. *Int. J. Numer. Meth. Fluids*, **43**:865–879 (2003).

[77] Takahashi, T. A wideband fast multipole accelerated boundary integral equation method for time-harmonic elastodynamics in two dimensions. *Int. J. Num. Meth. Eng.*, **91**:531–551 (2012).

[78] Takahashi, T., Cecka, C., Darve, E. Optimization of the parallel black-box fast multipole method on CUDA. In *Innovative Parallel Computing (InPar)* (2012). http://dx.doi.org/10.1109/InPar.2012.6339607.

[79] Takahashi, T., Nishimura, N., Kobayashi, S. A fast BIEM for three-dimensional elastodynamics in time domain. *Eng. Anal. Bound. Elem.*, **28**:165–180 (2004).

[80] Tanaka, M., Sladek, V., Sladek, J. Regularization techniques applied to boundary element methods. *Appl. Mech. Rev.*, **47**:457–499 (1994).

[81] Tausch, J. Sparse BEM for potential theory and Stokes flow using variable order wavelets. *Comp. Mech.*, **32**:312–3185 (2003).

[82] Tong, M.S., Chew, W.C. Multilevel fast multipole algorithm for elastic wave scattering by large three-dimensional objects. *J. Comp. Phys.*, **228**:921–932 (2009).

[83] Xiao, J., Ye, W., Cai, Y., Zhang, J. Precorrected FFT accelerated BEM for large-scale transient elastodynamic analysis using frequency-domain approach. *Int. J. Num. Meth. Eng.*, **90**:116–134 (2012).

[84] Yan, ZY, Zhang, J., Ye, W. Rapid solution of 3-D oscillatory elastodynamics using the pFFT accelerated BEM. *Eng. Anal. Bound. Elem.*, **34**:956–962 (2010).

[85] Ying, L., Biros, G., Zorin, D. A kernel-independent adaptive fast multipole in two and three dimensions. *J. Comp. Phys.*, **196**:591–626 (2004).

[86] Yoshida, K. I. *Application of fast multipole method to boundary integral equation method*. Ph.D. thesis, Kyoto University (2001).

[87] Zhao, J.-S., Chew, W. C. MLFMA for solving integral equations of 2-D electromagnetic problems from static to electrodynamic. *Microw. Opt. Technol. Lett.*, **20**:306–311 (1999).